EFFECT OF SUBSTRATE TYPE ON STRUCTURAL AND OPTICAL PROPERTIES OF METAL NANOPARTICLES FOR PLASMONIC APPLICATIONS

A THESIS SUBMITTED TO
THE GRADUATE SCHOOL OF NATURAL AND APPLIED SCIENCES
OF
MIDDLE EAST TECHNICAL UNIVERSITY

BY

İREM TANYELİ

IN PARTIAL FULFILLMENT OF THE REQUIREMENTS
FOR
THE DEGREE OF MASTER OF SCIENCE
IN
PHYSICS

AUGUST 2011

Approval of the thesis:

EFFECT OF SUBSTRATE TYPE ON STRUCTURAL AND OPTICAL PROPERTIES OF METAL NANOPARTICLES FOR PLASMONIC APPLICATIONS

Submitted by **İREM TANYELİ** in partial fulfillment of the requirements for the degree of **Master of Science Physics Department, Middle East Technical University** by,

Prof. Dr. Canan Özgen _____
Dean, Graduate School of **Natural and Applied Sciences**

Prof. Dr. Sinan Bilikmen _____
Head of Department, **Physics**

Prof. Dr. Raşit Turan _____
Supervisor, **Department of Physics, METU**

Assist. Prof. Dr. Alpan Bek _____
Co-Supervisor, **Department of Physics, METU**

Examining Committee Members:

Prof. Dr. Çiğdem Erçelebi _____
Department of Physics, METU

Prof. Dr. Raşit Turan _____
Department of Physics, METU

Assoc. Prof. Dr. Oğuz Gülseren _____
Department of Physics, Bilkent University

Assist. Prof. Dr. Alpan Bek _____
Department of Physics, METU

Assist. Prof. Dr. H. Emrah Ünalan _____
Department of Metallurgical Engineering, METU

Date: 25.08.2011

I hereby declare that all information in this document has been obtained and presented in accordance with academic rules and ethical conduct. I also declare that, as required by these rules and conduct, I have fully cited and referenced all material and results that are not original to this work.

Name, Last name : İREM TANYELİ

Signature :

ABSTRACT

EFFECT OF SUBSTRATE TYPE ON STRUCTURAL AND OPTICAL PROPERTIES OF METAL NANOPARTICLES FOR PLASMONIC APPLICATIONS

Tanyeli, İrem

M.Sc., Department of Physics

Supervisor: Prof. Dr. Raşit Turan

Co-supervisor: Assist. Prof. Dr. Alpan Bek

August 2011, 90 pages

In this work, the structural and optical properties of metal nanoparticles fabricated on various substrates have been investigated. The particles were fabricated by electron beam lithography (EBL) and dewetting of a thin metal film. The advantages and disadvantages of these two fabrication techniques are discussed by considering the properties of the nanoparticles and the applicability to large area substrates. Being a practical fabrication method, dewetting can be applied to any substrate with either small or large surfaces. For comparison between different sample types, some process parameters such as film thickness, annealing temperature and duration were fixed during the whole study. Gold (Au) and silver (Ag) were preferred for nanoparticle formation because of their superior optical properties for solar cell applications. We used silicon (Si), silicon nitride (Si_3N_4), silicon dioxide (SiO_2) and indium tin oxide (ITO) on glass, and textured Si as the substrate for the particle formation. These substrates are commonly used in solar cell technology for different purposes. The formation of the metal nanoparticles, their size and size distribution were monitored by Scanning Electron Microscope (SEM). We performed a dimension analysis on the SEM images using a program called Gwyddion. We observed that the substrate type

greatly affects particle mean size, suggesting a dependence of the dewetting process on the interface properties. Moreover, the effect of the annealing temperature was found to be a function of the substrate type.

Scattering measurements have been carried out in order to observe the localized surface plasmon resonance (LSPR) conditions. The effect of the particle size and the dielectric environment was observed as a shift in the plasmon resonance peak position along the wavelength axis. As expected from the theory, the resonance peaks shift to longer wavelengths with increasing particle size and dielectric constant. In order to compare the experimental results with the theory, Mie theory was applied to calculate the plasmon resonance peaks. We obtained fairly well agreement between the experimental and theoretical results. In this study, nanoparticles were assumed to be in contact with more than one medium, namely air and the underlying substrate.

Finally, we have reached a successful methodology and knowledge accumulation for the metal particle formation on variety of substrates by the dewetting technique. It is clear that this knowledge can form basis for the photovoltaic applications.

Keywords: Metal nanoparticles, localized surface plasmons, dewetting.

ÖZ

PLAZMONİK UYGULAMALARDA ALTTAŞ TÜRÜNÜN METAL NANO PARÇACIKLARIN YAPISAL VE OPTİK ÖZELLİKLERİNE ETKİSİ

Tanyeli, İrem

Yüksek Lisans, Fizik Bölümü

Tez Yöneticisi: Prof. Dr. Raşit Turan

Ortak tez yöneticisi: Assist. Prof. Dr. Alpan Bek

Ağustos 2011, 90 sayfa

Bu çalışmada, farklı alttaşlar üzerinde üretilmiş metal nano parçacıkların yapısal ve optik özellikleri incelenmiştir. Parçacıklar electron demet litografisi (EBL) ve ince metal film topaklanması yöntemi ile üretilmiştir. Nano parçacıkların özellikleri ve geniş alanlı alttaşlara uygulanabilirliği göz önüne alınarak bu iki üretim tekniğinin avantaj ve dezavantajları tartışılmıştır. Pratik bir üretim yöntemi olmasından ötürü topaklanma, küçük veya büyük yüzey alanına sahip herhangi bir alttaşa uygulanabilir. Farklı örnek türleri arasında kıyaslama yapabilmek için, film kalınlığı, tavlama sıcaklığı ve süresi gibi bazı işlem değişkenleri tüm çalışma sırasında sabit tutulmuştur. Güneş hücresi uygulamalarındaki üstün optik özelliklerinden dolayı nano parçacık oluşumunda altın (Au) ve gümüş (Ag) tercih edilmiştir. Parçacık oluşumda, silisyum (Si), silisyum nitrür (Si_3N_4), silisyum dioksit (SiO_2), indiyum kalay oksit (ITO) kaplı cam ve yüzeyi şekillendirilmiş Si alttaş olarak kullanılmıştır. Bu alttaşlar, güneş hücresi teknolojisinde farklı amaçlar için en yaygın olarak kullanılanlardır. Metal nano parçacık oluşumu, boyut ve boyut dağılımı taramalı alan mikroskopu (SEM) ile gözlenmiştir. Gwyddion adlı program kullanılarak SEM görüntüleri üzerinden boyut analizi yapılmıştır. Arayüz özelliklerine bağlı olarak, alttaş türünün

ortalama parçacık boyutunu büyük ölçüde etkilediği gözlemlenmiştir. Ayrıca, tavlama sıcaklığı etkisinin de alttaş türünün bir fonksiyonu olduğu bulunmuştur.

Lokalize yüzey plazmonlarının rezonans durumlarını gözlemleyebilmek için yansıma ölçümleri yapılmıştır. Parçacık boyutu ve yalıtkan çevrenin etkisi, rezonans tepe noktasının dalgaboyu ekseni üzerinde kaymalarıyla gözlemlenmiştir. Teoriden beklenildiği üzere, rezonans tepesi parçacık boyutunun ve yalıtkan sabitinin artmasıyla daha büyük dalgaboylarına doğru kaymıştır. Deneysel sonuçları teoriyle karşılaştırabilmek için plazmon rezonans tepeleri Mie teorisi uygulanarak hesaplanmıştır. Deneysel ve teorik sonuçlar arasında oldukça iyi bir örtüşme elde edilmiştir. Bu çalışmada, nano parçacıkların hava ve alttaş olmak üzere birden fazla ortamla temas halinde olduğu kabul edilmiştir.

En sonunda, topaklanma tekniğini kullanalarak farklı alttaşlar üzerinde metal nano parçacık oluşumu için başarılı bir yöntem ve bilgi birikimine erişilmiştir. Bu bilginin farklı güneş hücresi teknolojilerine uygulamalarına temel oluşturacağı açıktır.

Anahtar Kelimeler: Metal nanoparçacıklar, lokalize yüzey plazmonları, topaklanma.

To my mom and dad

ACKNOWLEDGEMENT

I would like to express my deepest thanks to my supervisor Prof. Dr. Raşit Turan for his guidance, help and patience. I would also like to thank my co-supervisor Assist. Prof. Dr. Alpan Bek for his valuable advice and supervision.

I would like to thank to the METU Central Laboratory and especially to Seçkin Öztürk and Sedat Canlı for SEM sessions. Discussions and advice from Mustafa Kulakçı, Serim İlday, Fırat Es and Urcan Güler was indispensable for me. I appreciate the help of Prof. Dr. Mehmet Parlak, Assist. Prof. Dr. Erman Bengü and Gökçe Küçükayan. I would like to thank to my group partners Mehmet Karaman, Olgu Demircioğlu, Zeynep Deniz Eygi, Yasin Ergunt, Nader A. P. Moghaddam, Gizem Nogay, Yücel Eke and my former and recent roommates Umut Bostancı and Makbule Bilgen for their friendly support.

I would also like to thank to my friends Berkcan Gökçe, Burçin İçdem, Serra Altınoluk and Kutlu Kutluer for their support and beautiful friendship.

I would like to thank to Scientific and Technological Research Council of Turkey (TUBITAK) for partial financial support during my graduate study.

Finally, I would like to express my endless thanks and gratitude to my mom and dad. Without their love, patience and support I would not have been able to complete this thesis.

TABLE OF CONTENTS

LIST OF FIGURES

FIGURES

LIST OF TABLES

TABLES

LIST OF ABBREVIATIONS

EBL	Electron Beam Lithography
SEM	Scanning Electron Microscope
FDTD	Finite Difference Time Domain
DDA	Discrete Dipole Approximation
PMMA	Poly (methyl methacrylate)
ITO	Indium Tin Oxide
MIBK	Methyl isobutyl ketone
IPA	Isopropyl alcohol
DI water	Deionized water
KOH	Potassium Hydroxide
AFM	Atomic Force Microscope
PECVD	Plasma Enhanced Chemical Vapor Deposition

CHAPTER 1

INTRODUCTION

1.1 History

History of plasmonics dates back to almost 2500 years ago, when the Egyptians and Romans used metal colloids in their household materials. The most famous example is the Lycurgus cup made by Romans 2400 years ago, which is a glass artifact having Au and Ag colloids on its surface. The Au (Au) and Ag (Ag) colloids embedded in the cup's surface cause unusual optical responses with various colors. This cup is not the only example from the history. Au or Ag colloids embedded in the glass windows of many cathedrals create colorful images expressing the scenes of religious events in the history.

It was Michael Faraday, who first scientifically engaged his intellect with the concept of plasmonics as early as 1857 [1]. He had discovered the differences in optical behavior of bulk and colloidal metals and attributed the color changes to the size of particles in nanoscale. In 1904, Maxwell Garnett improved the theory on optical behavior of metal nanoparticles embedded in glass and metal films [2]. Following this development, in 1908 Gustav Mie proposed a quantitative explanation for the interaction of metal nanoparticles with light by solving Maxwell's equations [3]. However, his theory is restricted in spherically symmetric particles. With the developments in the formation of metal nanoparticles, a need for a solution applicable to complex geometries was arisen. Several numerical methods such as Finite Difference Time Domain (FDTD) and Discrete Dipole Approximation (DDA) have been developed with the advancement in computer technology. After a long time from emerging of Mie theory, Otto and Kretschmann developed experimental configurations for excitation of surface plasmons in 1968 and 1971,

respectively [4, 5]. The plasmonics became popular in the last decades especially after the discovery of the enhancement effect of metal nanostructures on Raman scattering, which is known as the Surface Enhanced Raman Scattering (SERS) [6]. The number of studies on plasmonic applications has been increasing steadily since the first publications on SERS.

1.2 State of the art

There is a great variety in applications of plasmonic structures on light sensitive devices. One of the first examples was reported by Stuart and Hall on the enhancement of photocurrent in Si on insulator (SOI) photo detector with a thickness of 165 nm by plasmonic effects of Ag nanoparticles formed on the device by a dewetting process [7]. Schaadt et al. reached 50%-80% enhancement in the photocurrent of the Si pn junction diode at around plasmon resonance wavelength with Au nanoparticles [8]. After this study, Lim et al. worked on similar systems, which are Si photodiodes with Au nanoparticles and they also included finite element numerical simulation of these structures in their report [9]. Applications in various types of solar cells appear in the literature. Photocurrent and optical absorption enhancements were achieved with Ag nanoparticles with different deposition techniques in organic solar cells [10, 11]. Fahr et al. studied a model of a Si based tandem solar cell with Ag nanodiscs placed in an intermediate layer to increase the efficiency of the cell [12]. Hägglund et al. used Au discs which were fabricated by electron beam lithography (EBL) to enhance charge carrier generation for dye sensitized solar cell [13]. Scattering from metallic nanostructures were used to improve the performance of amorphous Si solar cells [14-16]. Complementary to the use of metal nanoparticles for enhancing the optical absorption, Si based light emitting diodes take advantage of electroluminescence enhancement of metal nanoparticles by incorporating them to their architecture [17-19]. In literature, studies of plasmonic enhancement by metal nanostructures are not only centered on the Si based devices. There are reports on light absorption enhancements for gallium arsenide (GaAs) [20, 21]. Photocurrent enhancements were also reported for several inorganic semiconductors such as cadmium selenide / silicon (CdSe/Si) by Konda et al. and indium phosphide / indium gallium arsenide phosphide (InP/InGaAsP) by Derkacs et al. [22, 23]. Apart from the standard geometries of metal nanostructures such as discs, Wurtz et al. reported a study on nanorod materials in plasmonic applications [24].

Pillai et al. evaporated Ag layer with thicknesses ranging from 14-27 nm and annealed under nitrogen (N_2) flow in order to obtain Ag nanoparticles [25]. The SEM results for these samples provided information on the effect of film thickness on particle formation. The particles fabricated in the study of Pillai et al. were not well ordered compared to the lithographic methods. Nevertheless, there are convincing studies on the integrability of this fabrication method to different applications [26, 27]. One of the important particle properties affecting the optical response is the geometry of the particles. Catchpole et al. compared the fraction of scattered light into the substrate from particles with various geometries [28]. Discovering the effect of dielectric layers and their thicknesses on the optical response of nanoparticles was among the main objectives of this and a number of their subsequent studies [28-30]. Because of limitations in the precise control during experiments and resulting uncertainties in the particle size and distribution, it is hard to demonstrate the expected features of the nanoparticles. For this reason, simulation studies are quite important to understand the plasmonic properties and predict possible applications. The most widely used and preferred numerical method is the FDTD, which was introduced by Yee in 1966 [29, 31-34]. Another most commonly used numerical method in the plasmonic studies is DDA which was proposed by Purcell and Pennypacker in 1973 [35].

1.3 Overview

In this work, metal nanostructures on various substrates have been fabricated using two different fabrication methods under controlled experimental conditions and the results have been analyzed. Different structures were produced by varying type of the metal and the substrate, the annealing temperature and the duration, and the annealing atmosphere. Au and Ag were preferred for nanoparticle formation because of their useful optical properties for solar cell applications. Substrates like Si, Si_3N_4, SiO_2, textured Si, ITO on glass and Si_3N_4 on textured Si are used for the particle formation. The effects of these variations on the nanoparticle formation and the optical responses were examined by measurements.

In Chapter 2, interaction of light with a particle is introduced. Subsequently, a theoretical analysis of the interaction is discussed for spherical particles in order to gain an insight on the plasmonic oscillations. The absorption and scattering from a spherical particle are evaluated by two approaches: the electrostatic approach and the Mie theory. The conditions

for the existence of localized modes are examined in order to understand the effect of the material design in plasmonic applications. In this analysis, we easily understand that the resonance condition for plasmonic particles is a strong function of the dielectric function. For this reason, the dielectric function is explained by two models, namely, Lorentz and Drude model. Although the concept of plasmonics has found a wide application niche, our interest is mainly focused on plasmonic solar cell properties. A short theoretical evaluation of the solar cell applications is introduced in this chapter. As mentioned above, the modeling of plasmonic applications is important, as the experimental studies should be explained accurately.

In Chapter 3, the experimental methods used in this thesis are described. As the fabrication methods, EBL and the dewetting of a thin film are explained in detail. EBL generates well defined particles and is preferred for highly sensitive analysis especially for the proof of principle studies. However, the maximum possible EBL area size, the fabrication cost, time and complexity forbiddingly limit its use in actual solar cell device production. On the other hand, for large area, cost effective and fast fabrication, self driven dewetting process is so far the most appropriate and therefore commonly used method.

After imaging the particles by SEM, a dimensional analysis was performed to characterize the size, shape and the surface coverage of the particles. This analysis is explained in Chapter 3. The experimental setup for the scattering measurements is also detailed in this chapter.

Chapter 4 presents the results on the structural and optical properties of the particles fabricated by the two methods. The size and shape analysis were done by statistical examinations carried out on the SEM images. Optical properties were derived from the scattering measurements. These experimental results and a comparison with those obtained from theoretical analysis are given in this chapter. Finally, the conclusions that we reached from this thesis work are presented in Chapter 5.

CHAPTER 2

THEORY OF OPTICAL PROPERTIES OF SOLIDS WITH REDUCED DIMENSIONS

In the introduction part, various application fields that take advantage of plasmonic oscillations for device efficiency enhancements with both far field and near field effects were discussed. To gain insight on mechanisms governed by localized surface plasmons generated when confined in metal nanostructures, the light interaction with particles should be discussed. The most important process that can take place during device operation is the absorption and scattering in the surface region of the device whose performance can hopefully be improved by nanostructures formed on the surface. However, to conceive the main ideas and the tricky points in plasmonic concept and its applications, some basic physical phenomena should be understood. In the following subsection, the absorption and scattering processes are summarized with plasmonic perspective.

2.1 Absorption and scattering by a particle

From a general point of view, the scattering mechanism from any system is attributed to its heterogeneity. The obstacle in that system which is subjected to an illumination by an electromagnetic wave could be even a single electron, an atom, a solid or liquid particle. Regardless of the type of the obstacle, they can be generalized as a matter consisting of electrons and protons. As the obstacle is illuminated by an electromagnetic wave, its electric charges tend to go in an oscillatory motion with electric field. The electric charges that are accelerated throughout the illumination scatter electromagnetic energy. The scattering by the

obstacle is considered as a secondary radiation which is in all directions and it can be summarized as:

$$Scattering = Excitation + Reradiation$$

In addition to scattering, one more mechanism occurs in the obstacle. The excited electric charges could also convert some part of the incident electromagnetic energy into other forms, most conventionally to thermal energy. This process is called absorption. Those two processes should not be considered as independent from each other.

The absorption and scattering characteristics of particles under a definite illumination may differ totally from each other according to their size, shape and structural composition. However, it is still possible to make some generalizations for the concept of scattering and absorption by small particles.

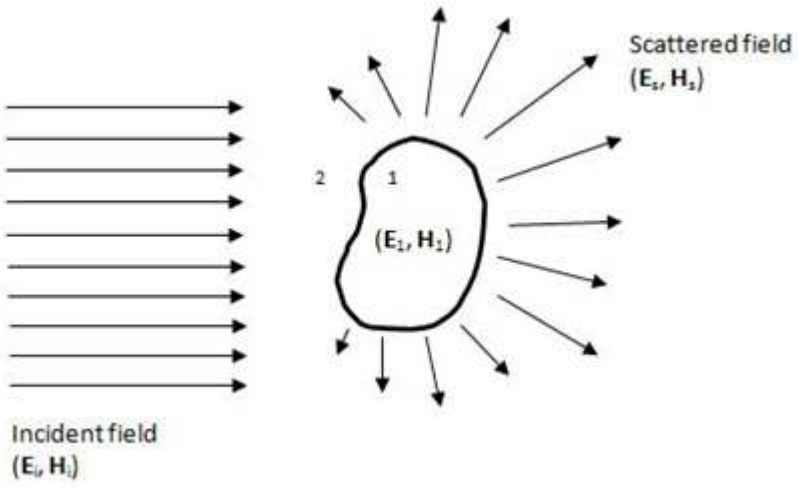

Figure 2.1.1 : Incident electromagnetic field gives rise to fields inside and outside of the particle

To distinguish the electromagnetic fields inside and outside the particle, lets denote the fields inside as $(\boldsymbol{E_1}, \boldsymbol{H_1})$ and outside as $(\boldsymbol{E_2}, \boldsymbol{H_2})$ which is the superposition of the incident $(\boldsymbol{E_i}, \boldsymbol{H_i})$ and scattered field $(\boldsymbol{E_s}, \boldsymbol{H_s})$, as illustrated in Figure 2.1.1. In continuous media the electromagnetic fields are expected to satisfy the Maxwell's equations. However, in the present case, there is a discontinuity when passing form particle surface to medium which means that $\in$ and μ are changing through that boundary. For such cases the condition for the fields is as follows:

$$[\boldsymbol{E}_2(\boldsymbol{x}) - \boldsymbol{E}_1(\boldsymbol{x})] \times \hat{\boldsymbol{n}} = 0 \quad 2.1.1$$

$$[\boldsymbol{H}_2(\boldsymbol{x}) - \boldsymbol{H}_1(\boldsymbol{x})] \times \hat{\boldsymbol{n}} = 0 \quad 2.1.2$$

where $\hat{\boldsymbol{n}}$ is the outward directed normal to the surface of the particle. Equations above denote that the tangential components of $\boldsymbol{E}$ and $\boldsymbol{H}$ are continuous at the boundary of the particle and medium. Moreover, the rates at which electromagnetic energy is transferred across a closed surface are given below:

$$\int \boldsymbol{S}_1 \cdot \hat{\boldsymbol{n}} dA = \int \hat{\boldsymbol{n}} \cdot (\boldsymbol{E}_1 \times \boldsymbol{H}_1) dA \quad 2.1.3$$

$$\int \boldsymbol{S}_2 \cdot \hat{\boldsymbol{n}} dA = \int \hat{\boldsymbol{n}} \cdot (\boldsymbol{E}_2 \times \boldsymbol{H}_2) dA \quad 2.1.4$$

where 1 and 2 denotes inner and outer surfaces, respectively. With the relations given in equations 2.1.1 and 2.1.2 the rates are equalized as

$$\int \boldsymbol{S}_1 \cdot \hat{\boldsymbol{n}} dA = \int \boldsymbol{S}_2 \cdot \hat{\boldsymbol{n}} dA$$

which means that the energy is conserved across the boundary.

From the pedagogical point of view, suppose that a particle is embedded in a medium under radiation. The power is expected to change after passing the particle because of extinction of the incident radiation. The difference in power is attributed to the absorption in particle and scattering by particle in a nonabsorbing medium. These processes have the following relation under energy transfer rates:

$$W_{ext} = W_a + W_s \quad 2.1.5$$

The ratio of energy rates corresponding to the relevant process to incident irradiance gives the cross section terms. The optical cross section of a particle is one of the most significant and descriptive parameter in concept of plasmonics.

$$C_{sca} = \frac{W_s}{I_i}, C_{abs} = \frac{W_{abs}}{I_i}, C_{ext} = \frac{W_{ext}}{I_i} \quad 2.1.6$$

However that cross section is not same as the geometrical cross section which is related to the collisions. The relation between the energy transfer rates for extinction, absorption and scattering mechanisms holds for their cross section term [36].

$$C_{ext} = C_{abs} + C_{sca} \qquad 2.1.7$$

In the following sections, the expansion of each cross section terms is given under various conditions.

In this section, the absorption and scattering processes are discussed from a general point of view. The light interaction with metal nanoparticles, which is the main topic of this study, is analyzed in the next section.

2.2 Absorption and scattering by a sphere

For simplicity, it would be beneficial to consider a model of a metal sphere. In equilibrium, free electrons move against immobile positive ions in the case that both have the same density. However, an illumination may disturb this equilibrium condition by changing the charge distribution in the system.

The conduction electrons in a metal particle oscillate with the oscillating electric field component of the electromagnetic wave under the light irradiation. During this oscillation, the electron cloud is shifted relative to the nuclei (see Figure 2.2.1). The frequency of the oscillation is directly affected by the density of electrons, the effective electron mass, the shape and the size of the charge distribution [37].

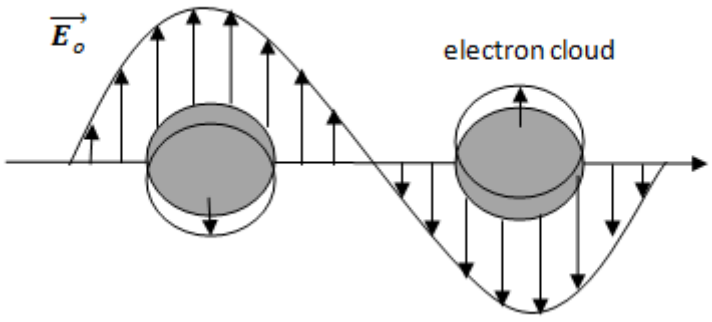

Figure 2.2.1 : Displacement of the electron cloud relative to the nuclei during plasmon oscillation is shown

Let us now focus on the effect of metal nanoparticle's size on electron oscillation. As mentioned above, the electrons oscillate with the incident electric field. That collective

oscillation could be coherent and incoherent according to the size of the particle. If the collective oscillation is coherent, the dipole modes dominantly govern the oscillation. This mode is called the dipole plasmon resonance or dipole particle plasmon resonance. When the particle size increases higher order modes such as quadrupole, octupole modes can be induced. In those cases, half of the electrons move parallel to the incident electric field and the other half move antiparallel.

In the following sections, the plasmon resonances for spherical particles are evaluated with two basic approaches; electrostatic and Mie theory as a function of the size of the spherical metal particles.

2.2.1 Electrostatic Approach

For metal nanoparticles whose dimensions are less than about 10% of the wavelength of light, the electric field of the incident irradiation can be considered as constant. Under that condition, the interaction of light with particle is evaluated under the principles of the electrostatics rather than the electrodynamics. This approach can be named as quasistatic approximation or Rayleigh scattering by a small particle.

As denoted before, the electric field can be regarded as constant, so the electric field of the incident radiation is indicated as $\boldsymbol{E}_0$ in the x-direction in Cartesian coordinates; $\boldsymbol{E}_0 = E_0\hat{x}$ (see Figure 2.2.2).

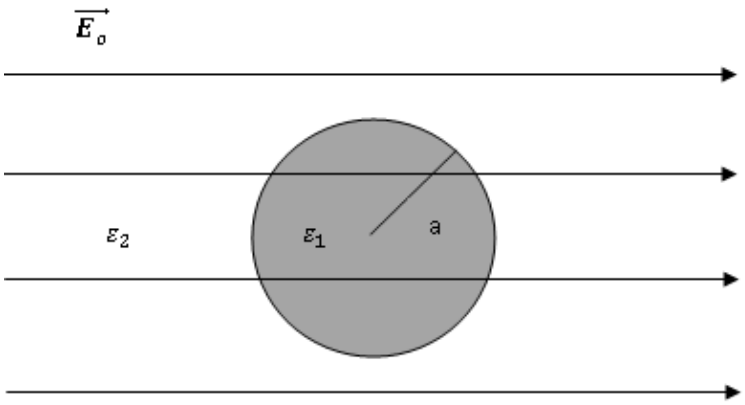

Figure 2.2.2 : Spherical particle in uniform electric field

To obtain the electric field inside and outside of the small spherical particle, the fundamental equation of electrostatics, which is the Laplace's equation, should be solved in spherical coordinates (r, θ, φ) [38].

$$\frac{1}{r^2}\frac{\partial}{\partial r}\left(r^2\frac{\partial \Phi}{\partial r}\right)+\frac{1}{r^2\sin\theta}\frac{\partial}{\partial \theta}\left(\sin\theta\frac{\partial \Phi}{\partial \theta}\right)+\frac{1}{r^2 sin^2\theta}\frac{\partial^2 \Phi}{\partial \varphi^2}=0 \qquad 2.2.1$$

This step comes from the requirement that the electric potential which is related to electric field by $\boldsymbol{E}=-\nabla\Phi$ must satisfy the Laplace's equation

$$\nabla^2\Phi=0 \qquad 2.2.2$$

The general form of the solution for electric potential is

$$\Phi(r,\theta,\varphi)=\sum_{l,m} b_{l,m}\cdot\begin{Bmatrix} r^{l} \\ r^{-l-1}\end{Bmatrix}\begin{Bmatrix} P_l^m(\cos\theta) \\ Q_l^m(\cos\theta)\end{Bmatrix}\begin{Bmatrix} e^{im\varphi} \\ e^{-im\varphi}\end{Bmatrix} \qquad 2.2.3$$

Here, $b_{l,m}$ will be obtained from boundary conditions and the terms represented as $P_l^m(\cos\theta)$ and $Q_l^m(\cos\theta)$ are the associated with Legendre functions and the Legendre functions of the second kind, respectively. In the present consideration, it is possible to get rid of the φ dependence by azimuthal symmetry assumption.

One should pay attention to the fact that the potential at the origin has to be finite. By taking that constraint into account, the potential inside (Φ_1) and outside of the particle (Φ_2) could be simplified as

$$\Phi_1(r,\theta)=\sum_{l=0}^{\infty}A_l r^l P_l(\cos\theta) \qquad 2.2.4$$

$$\Phi_2(r,\theta)=\sum_{l=0}^{\infty}\left[B_l r^l+C_l r^{-(l+1)}\right]P_l(\cos\theta) \qquad 2.2.5$$

The crucial point for the potential outside of the particle is that at infinite distance it has to converge to $-E_0 r\cos\theta$.

In order to reach exact solutions, two boundary conditions should be applied by considering the constraints for potentials at both regions.

$$\left[\frac{\partial \Phi_1}{\partial \theta}\right]_{r=a} = \left[\frac{\partial \Phi_2}{\partial \theta}\right]_{r=a} \quad 2.2.6$$

$$\varepsilon_1 \left[\frac{\partial \Phi_1}{\partial r}\right]_{r=a} = \varepsilon_2 \left[\frac{\partial \Phi_2}{\partial r}\right]_{r=a} \quad 2.2.7$$

where a is the radius of the spherical particle. The potential outside of the particle can be written as

$$\Phi_2 = \Phi_{scatter} + \Phi_0 \quad 2.2.8$$

where $\Phi_{scatter}$ and Φ_0 are the potentials of incoming and scattered fields, respectively. In this case incoming potential is $\Phi_0 = -E_0\hat{x}$.

After the application of all boundary conditions and constraints, the potentials have the form

$$\Phi_1 = -E_0 \frac{3\varepsilon_2}{\varepsilon_1 + 2\varepsilon_2} r\cos\theta \quad 2.2.9$$

$$\Phi_2 = -E_0 r\cos\theta + E_0 \frac{\varepsilon_1 - \varepsilon_2}{\varepsilon_1 + 2\varepsilon_2} a^3 \frac{\cos\theta}{r^2} \quad 2.2.10$$

By using the relation $\boldsymbol{E} = -\nabla\Phi$ the electric field can be derived from potential as

$$\boldsymbol{E}_1 = E_0 \frac{3\varepsilon_2}{\varepsilon_1 + 2\varepsilon_2}\left(\cos\theta\,\hat{r} - \sin\theta\,\hat{\theta}\right) = E_0 \frac{3\varepsilon_2}{\varepsilon_1 + 2\varepsilon_2}\hat{x} \quad 2.2.11$$

$$\boldsymbol{E}_2 = E_0\left(\cos\theta\,\hat{r} - \sin\theta\,\hat{\theta}\right) + \frac{\varepsilon_1 - \varepsilon_2}{\varepsilon_1 + 2\varepsilon_2}\frac{a^3}{r^3}E_0\left(2\cos\theta\,\hat{r} + \sin\theta\,\hat{\theta}\right) \quad 2.2.12$$

When the electric fields above are analyzed carefully, some particular points should be considered. The electric field inside the spherical particle is found to be homogenous. This is an unexpected result, since the electromagnetic field in metals decays exponentially. For this reason, in the case of quasistatic approximation the particles are smaller in size than the skin depth (d) of the metal, where $d = \lambda/\left(4\pi\sqrt{\varepsilon}\right)$. The other specific point is related to the field outside the particle. The first term in $\boldsymbol{E}_2$ is the applied field and the second term is the induced dipole field which is generated by a dipole centered at the origin of the sphere. Analogically the potential outside the particle can be reformed as

$$\Phi_2 = -E_0 r\cos\theta + \frac{\boldsymbol{p}\cdot\boldsymbol{r}}{4\pi\varepsilon_0\varepsilon_2 r^3} \quad 2.2.13$$

where the dipole moment of the dipole is

$$\boldsymbol{p} = 4\pi\varepsilon_0\varepsilon_2 \frac{\varepsilon_1 - \varepsilon_2}{\varepsilon_1 + 2\varepsilon_2} a^3 \boldsymbol{E}_0 \qquad 2.2.14$$

Since the relation between dipole moment and applied electric field is known as $\boldsymbol{p} = \varepsilon_2 \alpha(\omega) \boldsymbol{E}_0$, the polarizability can be defined by

$$\alpha(\omega) = 4\pi\varepsilon_0 a^3 \frac{\varepsilon_1(\omega) - \varepsilon_2}{\varepsilon_1(\omega) + 2\varepsilon_2} \qquad 2.2.15$$

The polarizability is the most significant parameter for the main subject of this work. This term gives an idea of resonance condition and its dependencies. As the denominator of the polarizability may approach zero under specific conditions, the particle resonates and the electric field around the particle may enhance strongly. As seen from the above equation, the resonance condition is directly related to the choice of both surrounding medium and the material for the sphere. However, in plasmonic applications metal nanoparticles are placed in a dielectric medium. The metals are known to have complex dielectric functions with negative real part. The dielectric function of them is also highly frequency dependent and should be represented as a function of frequency. On the other hand, dielectrics have positive real dielectric functions. As can easily be figured out by considering the denominator of the polarizability, the complex part of the $\varepsilon_1(\omega)$ leads to a reduction in the electric field enhancement around the particle.

The reasons of the material type selection for both surrounding medium and particle and also the dielectric function behaviors with frequency dependencies are discussed in the following sections.

In section 2 the cross section terms are explained, where their meanings are clarified. They can be obtained from the division of total radiated power of the sphere's dipole with the intensity of the exciting plane wave. As a result the scattering cross section is

$$C_{sca} = \frac{k^4}{6\pi{\varepsilon_0}^2} |\alpha(\omega)|^2 \qquad 2.2.16$$

As mentioned earlier, the power of the incident beam dissipates not only due to scattering by the particle, but also due to absorption by it. The sum of the both processes is called the extinction. Similar to the scattering case, the absorption cross section is obtained by dividing

the power dissipated by a point dipole with the intensity of the exciting plane wave, and can be found as

$$C_{abs} = \frac{k}{\varepsilon_0} Im[\alpha(\omega)] \qquad 2.2.17$$

The size effect in the particle-light interactions should be discussed. In the extended form of the polarizability shown above, it is recognized that polarizability is proportional to size of the particle. Moreover, the scattering cross section scales with a^6 and the absorption cross section scales with a^3. Consequently, it is then clear that the scattering mechanism is much more dominant in extinction rather than absorption for larger particles. Accordingly, the size of the particle should be chosen carefully for specific applications.

Before the application of the boundary conditions to evaluate the exact solution for the electric potential, the general forms of potentials should be considered. The potential inside the particle has radial dependence as r^l and outside as $r^{-(l+1)}$ where l is the angular momentum. Up to now, the dipole plasmon resonance condition has been taken into to the consideration where $l = 1$ leading to the radial solutions in the form of r and r^{-2}. However, for the larger particles the quadrupole terms resulting from $l = 2$, should also be included in the solution of the Laplace's equation. Consequently, the quadrupole polarizability is obtained as

$$\beta = 4\pi\varepsilon_0 a^5 \frac{\varepsilon_1(\omega) - \varepsilon_2}{\varepsilon_1(\omega) + 3/2\varepsilon_2} \qquad 2.2.18$$

This approach is not good enough to define the resonance condition for particles with diameter larger than 40 nm in the visible region. On the other hand, it is useful to get qualitative information about the resonance. For a more detailed and quantitative analysis, new approaches are needed. The Mie theory, which is described below, has been used satisfactorily for this purpose.

2.2.2 Mie Theory

In the preceding section, particles in sizes smaller than the wavelength of the incident light were covered through an electrostatic approach. In this section, the scope is shifted to particles having sizes even in the order of the wavelength of the incident beam. The first

interest to this topic had arisen for the color variations in the absorption and scattering caused by small Au colloidal particles suspended in water. In 1908, Gustav Mie presented a solution to explain this observation. Although the science of metal nanoparticles has evolved through the years and new methods have been developed successfully, Mie theory has preserved its importance up to now. The reason of it may be that it is the only simple and exact solution to Maxwell's equations for small particles [37]. Moreover, the Mie theory explains the spherical particles in any size unlike theories like Maxwell-Garnet theory. However, the theory has a drawback; it is only applicable to the spherical particles. For the nanoparticles fabricated by lithographic methods with spherical shape, Mie theory gives the extinction spectra with very high accuracies.

The starting point of the theory is to solve Maxwell's equation for light represented as plane wave scattered from a spherical particle [39]. Consequently, it is possible to deal with a time-harmonic electromagnetic field in a linear, isotropic and homogenous medium. The field should satisfy the wave equation with zero divergence as

$$\nabla^2 \boldsymbol{E} + k^2 \boldsymbol{E} = 0 \qquad 2.2.19$$

$$\nabla^2 \boldsymbol{H} + k^2 \boldsymbol{H} = 0 \qquad 2.2.20$$

With an analogy to electromagnetic field represented above, a divergence free vector function $\boldsymbol{M}$ is generated as

$$\boldsymbol{M} = \nabla \times (\boldsymbol{c}\psi) \qquad 2.2.21$$

where $\boldsymbol{c}$ is an arbitrary constant vector or called as guiding vector and ψ is a scalar function.

By applying the vector identities for $\nabla \times (\boldsymbol{A} \times \boldsymbol{B})$ and $\nabla(\boldsymbol{A} \cdot \boldsymbol{B})$ to the vector function $\boldsymbol{M}$, the following equation is obtained

$$\nabla^2 \boldsymbol{M} + k^2 \boldsymbol{M} = \nabla \times [\boldsymbol{c}(\nabla^2 \psi + k^2 \psi)] \qquad 2.2.22$$

In the case, where ψ is a scalar wave equation as a solution, then $\boldsymbol{M}$ directly satisfies the vector wave equation.

One step further, another vector function $\boldsymbol{N}$ is generated from $\boldsymbol{M}$ by preserving the same requirements such as zero divergence and vector wave equation satisfaction.

$$\boldsymbol{N} = \frac{\nabla \times \boldsymbol{M}}{k} \qquad 2.2.23$$

As a result, it would not be wrong to say that $\boldsymbol{M}$ and $\boldsymbol{N}$ have all prerequisite properties same as an electromagnetic field. Therefore, the problem is simplified to solve for a scalar wave equation. The scalar function ψ is called a generating function for the vector harmonics $\boldsymbol{M}$ and $\boldsymbol{N}$.

A complete description of the theory requires a lengthy derivation with complicated equations. Nevertheless, the brief information given above is sufficient to gain an insight on the origin of the idea behind the Mie theory.

The general solution for ψ can be derived from the scalar wave equation

$$\nabla^2\psi + k^2\psi = 0 \qquad 2.2.24$$

by applying the boundary conditions at the surface of the sphere, which implies that the tangential components of $\boldsymbol{E}$ and $\boldsymbol{H}$ which are derived from ψ have to be continuous. The solutions are given below

$$\psi_{emn} = \cos m\emptyset \, P_n^m(\cos\theta) z_n(kr) \qquad e: even \qquad 2.2.25$$

$$\psi_{omn} = \sin m\emptyset \, P_n^m(\cos\theta) z_n(kr) \qquad o: odd \qquad 2.2.26$$

where z_n is a spherical Bessel function, $m = 0, \pm1, \pm2, \ldots, \pm n$ and $n = 0, 1, 2, \ldots.$. From these solutions it is now possible to construct incident electric and magnetic fields using the relations $\boldsymbol{M}_{emn} = \nabla \times \boldsymbol{r}\psi_{emn}$ and $\boldsymbol{N}_{emn} = k^{-1}\{\nabla \times \boldsymbol{M}_{emn}\}$ where $\boldsymbol{M}_{emn}$ and $\boldsymbol{N}_{emn}$.

$$\boldsymbol{E_i} = E_0 \sum_{n=1}^{\infty} i^n \frac{2n+1}{n(n+1)} (\boldsymbol{M_{o1n}^{(1)}} - i\boldsymbol{N_{e1n}^{(1)}}) \qquad 2.2.27$$

$$\boldsymbol{H_i} = \frac{-k}{\omega\mu} E_0 \sum_{n=1}^{\infty} i^n \frac{2n+1}{n(n+1)} (\boldsymbol{M_{e1n}^{(1)}} - i\boldsymbol{N_{o1n}^{(1)}}) \qquad 2.2.28$$

Again the boundary condition at the sphere surface should hold for the derivations of fields inside the sphere and scattered field by the particle. The fields inside the sphere $\boldsymbol{E_1}$ and $\boldsymbol{H_1}$ are

$$\boldsymbol{E_1} = E_0 \sum_{n=1}^{\infty} i^n \frac{2n+1}{n(n+1)} (c_n \boldsymbol{M_{o1n}^{(1)}} - i d_n \boldsymbol{N_{e1n}^{(1)}}) \quad 2.2.29$$

$$\boldsymbol{H_1} = \frac{-k}{\omega\mu} E_0 \sum_{n=1}^{\infty} i^n \frac{2n+1}{n(n+1)} (d_n \boldsymbol{M_{e1n}^{(1)}} - i c_n \boldsymbol{N_{o1n}^{(1)}}) \quad 2.2.30$$

The coefficients of the field inside the particle are solved from linear equation in the frame of the theory as

$$c_n = \frac{\mu_1 j_n(x) \left[x h_n^{(1)}(x)\right]' - \mu_1 h_n^{(1)} [x j_n(x)]'}{\mu_1 j_n(mx) \left[x h_n^{(1)}(x)\right]' - \mu h_n^{(1)}(x) [mx j_n(mx)]'} \quad 2.2.31$$

$$d_n = \frac{\mu_1 m j_n(x) \left[x h_n^{(1)}(x)\right]' - \mu_1 m h_n^{(1)} [x j_n(x)]'}{\mu m^2 j_n(mx) \left[x h_n^{(1)}(x)\right]' - \mu_1 h_n^{(1)}(x) [mx j_n(mx)]'} \quad 2.2.32$$

where μ_1 is the permeability of the sphere and $\mu = cos\theta$. The scattered fields are also derived from boundary condition as

$$\boldsymbol{E_s} = E_0 \sum_{n=1}^{\infty} i^n \frac{2n+1}{n(n+1)} (i a_n \boldsymbol{N_{e1n}^{(3)}} - b_n \boldsymbol{M_{o1n}^{(3)}}) \quad 2.2.33$$

$$\boldsymbol{H_s} = \frac{k}{\omega\mu} E_0 \sum_{n=1}^{\infty} i^n \frac{2n+1}{n(n+1)} (i b_n \boldsymbol{N_{o1n}^{(3)}} + a_n \boldsymbol{M_{e1n}^{(3)}}) \quad 2.2.34$$

and the scattering coefficients are

$$a_n = \frac{\mu m^2 j_n(mx) [x j_n(x)]' - \mu_1 j_n(x) [mx j_n(mx)]'}{\mu m^2 j_n(mx) \left[x h_n^{(1)}(x)\right]' - \mu_1 h_n^{(1)}(x) [mx j_n(mx)]'} \quad 2.2.35$$

$$b_n = \frac{\mu_1 j_n(mx) [x j_n(x)]' - \mu j_n(x) [mx j_n(mx)]'}{\mu_1 j_n(mx) \left[x h_n^{(1)}(x)\right]' - \mu h_n^{(1)}(x) [mx j_n(mx)]'} \quad 2.2.36$$

where the size parameter x and the relative refractive index m are

$$x = ka = \frac{2\pi n a}{\lambda}, m = \frac{N_1}{N}$$

a is the radius of the sphere, N_1 and N are the refractive indices of sphere and the medium, respectively.

After these derivations, we can now define the cross sections for the spherical particle as

$$C_{sca} = \frac{W_s}{I_i} = \frac{2\pi}{k^2}\sum_{n=1}^{\infty}(2n+1)(|a_n|^2 + |b_n|^2) \quad 2.2.37$$

$$C_{ext} = \frac{W_{ext}}{I_i} = \frac{2\pi}{k^2}\sum_{n=1}^{\infty}(2n+1)Re\{a_n + b_n\} \quad 2.2.38$$

The absorption cross section can be obtained from the constitutive relation between the other cross sections.

$$C_{abs} = C_{ext} - C_{sca} \quad 2.2.39$$

The cross sections were solved from two approaches, electrostatic approach and Mie theory. In the article of Kelly et al., they have compared these approaches on extinction efficiency calculation [37]. The extinction efficiency is the ratio of extinction cross section to the geometrical cross section of sphere. The calculations were carried out for spheres whose radii were 30 nm and 60 nm. In Figure 2.2.3, the results obtained from two approaches were plotted.

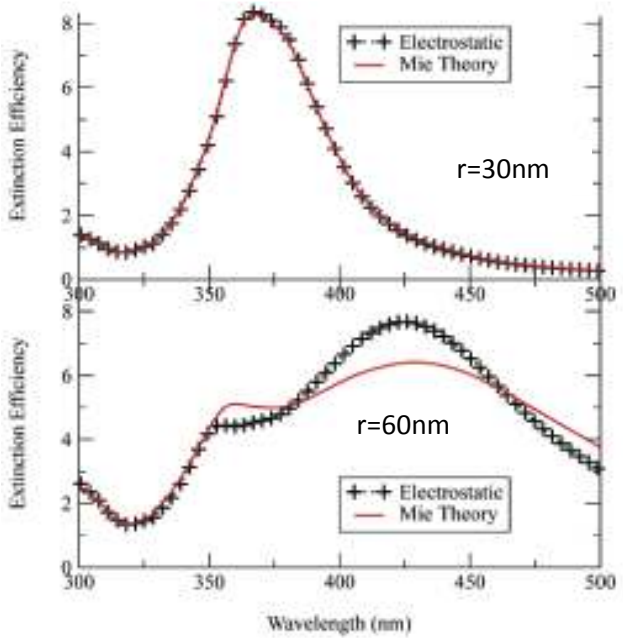

Figure 2.2.3 : Extinction efficiencies are plotted from both electrostatic and Mie theory for Ag sphere whose radius is 30 nm and 60 nm, respectively. [37]

The peaks in the extinction efficiencies, which were calculated for sphere with 30 nm radius from two approaches, perfectly matched. That peak is attributed to the dipole peak. However, the form of the extinction efficiency was changed as the radius of the sphere was increased to 60 nm. The dipole peak was redshifted and broadened relative to the previous case. Moreover, a quadrupole peak became noticeable. Distinctly from the calculations for the sphere with 30 nm radius, the results obtained from two approaches differ from each other; however, the main behavior was preserved. Even though the calculation of Mie theory is easily accessible, electrostatic approach is appropriate to get a qualitative result.

2.3 Surface Plasmon Polariton at Plane Interfaces

The most crucial mechanisms for plasmonic concept take place at the interfaces in the localized forms. For this reason, the homogenous solution for the Maxwell's equations at the interface is of great interest. For this particular case, the following wave equation should be solved [40].

$$\nabla \times \nabla \times E(r,\omega) - \frac{\omega^2}{c^2}\varepsilon(r,\omega)E(r,\omega) = 0 \qquad 2.3.1$$

Just for visualization, the interface is considered to lie at z=0 plane (see Figure 2.3.1). For the $z < 0$ region the dielectric function ε_1 is taken to be complex and for the $z > 0$ region ε_2 to be real.

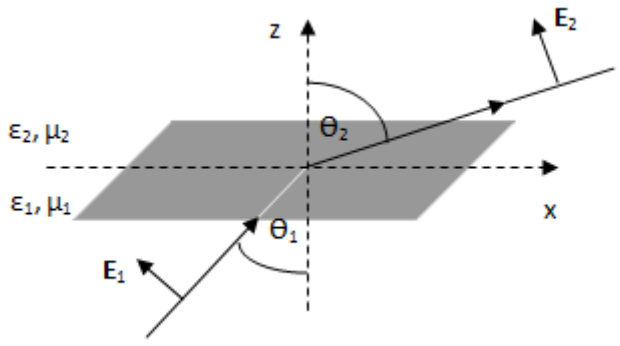

Figure 2.3.1 : Interface between two medium with dielectric functions ε_1 and ε_2

Plane waves for the both half is written as

$$E_i = \begin{pmatrix} E_{j,x} \\ 0 \\ E_{j,z} \end{pmatrix} e^{ik_x x - i\omega t} e^{ik_{j,z} z} \quad \text{j=1, 2} \tag{2.3.2}$$

where j represents the lower $(j = 1)$ and upper $(j = 2)$ parts of the interface. From the Maxwell's equations it is known that the parallel component of the wavevectors to the interface is conserved; thus the relation for the wavevectors comes out as follows:

$$k_x{}^2 + k_{j,z}{}^2 = \varepsilon_j k^2 \tag{2.3.3}$$

As the two halves of the interface are assumed to be source free, which means that $\nabla \cdot \boldsymbol{D} = 0$, the following equation is derived:

$$k_x E_{j,x} + k_{j,z} E_{j,z} = 0 \tag{2.3.4}$$

These relations lead us to write the plane waves in simpler form as follows:

$$E_j = E_{j,x} \begin{pmatrix} 1 \\ 0 \\ -k_x/k_{j,z} \end{pmatrix} e^{ik_{j,z} z} \tag{2.3.5}$$

By combining the requirements of continuity of parallel components of E and the perpendicular components of D at the interface with equation 2.3.4, we find

$$\varepsilon_1 k_{2,z} - \varepsilon_2 k_{1,z} = 0 \tag{2.3.6}$$

Furthermore, equations 2.3.3 and 2.3.6 help to form relations for k_x andk_z.

$$k_x{}^2 = \frac{\varepsilon_1 \varepsilon_2}{\varepsilon_1 + \varepsilon_2} k^2 \tag{2.3.7}$$

$$k_{j,z}{}^2 = \frac{\varepsilon_j{}^2}{\varepsilon_1 + \varepsilon_2} k^2 \tag{2.3.8}$$

Since all the background relations have been derived, it is time to deal with the conditions for interface mode to exist. Under the assumption that the imaginary parts of the dielectric functions are negligible when compared with the real parts, the requirements to have a bound solution are in the following.

$$\varepsilon_1 \cdot \varepsilon_2 < 0 \tag{2.3.9}$$

$$\varepsilon_1 + \varepsilon_2 < 0 \qquad 2.3.10$$

The only condition to hold these relations is that one of the dielectric functions is negative and dominates the dielectric function. Therefore, from the dielectric function characteristics of materials, it is easily concluded that a metal and dielectric interface provides localized modes. Actually, by this argument, it is clear why the experimentalists are interested in the plasmonics at the dielectric and metal interfaces of the devices.

2.4 Theories of Optical Constants

As the main subject of this work is related to the interaction of matter with light, the basic theories on optical constants and the optical properties of the materials should be covered thoroughly for a better understanding of the observed phenomena.

There are two parameters used alternatively to describe the optical properties of a material, namely complex refractive index $N = n + ik$ and complex dielectric function $\epsilon = \epsilon' + i\epsilon^{"}$. The relation between the two quantities for a nonmagnetic material is given as;

$$\in' = n^2 - k^2 \qquad 2.4.1$$

$$\in^{"} = 2nk \qquad 2.4.2$$

Depending on the application, one chooses one of these parameters. For example, the complex refractive index is used when the wave propagation is considered. On the other hand, for the microscopic mechanisms of a material, the complex dielectric function is preferred [36]. Since in this work the absorption and scattering by metal nanoparticles are studied, the complex dielectric function is more appropriate parameter for a clearer description of the system.

The calculation of complex dielectric function for metals could be made clearer by constitutive relations in equations 2.4.3 and 2.4.4 for a particle in an electric field. The electrons tend to move by r in the presence of an electric field. This displacement leads to creation of a dipole moment and the collective effect of the dipole moment of free electrons is the formation of a macroscopic polarization per unit volume. The polarization, denoted by $\boldsymbol{P}$, can be represented by;

$$\boldsymbol{P}(\omega) = \varepsilon_0 \chi_e(\omega) \boldsymbol{E}(\omega) \quad 2.4.3$$

where $\chi_e(\omega)$ is the susceptibility. For a nondispersive linear and isotropic medium, the electric displacement is expressed as

$$\boldsymbol{D}(\omega) = \varepsilon_0 \varepsilon(\omega) \boldsymbol{E}(\omega) = \varepsilon_0 \boldsymbol{E}(\omega) + \boldsymbol{P}(\omega) \quad 2.4.4$$

From those constitutive relations complex dielectric function can be simplified to

$$\varepsilon(\omega) = 1 + \chi_e(\omega) \quad 2.4.5$$

Now, it is straightforward to calculate the complex dielectric function. In order to obtain this displacement from the equation of motion for electrons under the electric field should be solved. Therefore, polarization and susceptibility are evaluated to complete the calculation [40].

2.4.1 Lorentz Model

The simple harmonic oscillator model is used in many branches of modern physics, since it can be applied for describing various phenomena [41]. For this reason, the simple harmonic oscillator model was preferred by Lorentz to reach the optical dielectric constants of a solid material at the beginning of this century. This model is briefly described below and illustrated in Figure 2.4.1.

In a classical approach, the electrons and ions of matter modeled as a simple harmonic oscillator under an external electromagnetic field.

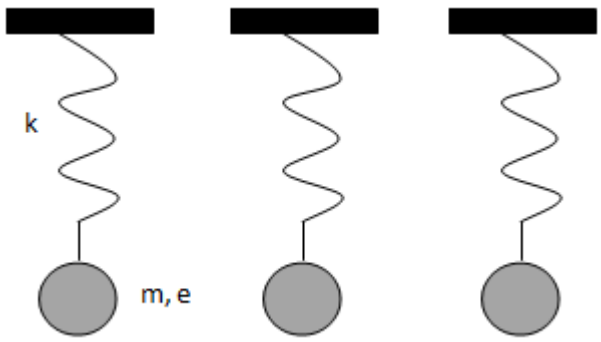

Figure 2.4.1 : Simple harmonic oscillators used to solve dielectric functions from Lorentz model.

The equation of motion for an oscillator with a spring constant K and a damping constant b can be constructed as;

$$m\ddot{\boldsymbol{x}} + b\dot{\boldsymbol{x}} + K\boldsymbol{x} = e\boldsymbol{E}_{local} \tag{2.4.1}$$

where m and e are the effective mass and the charge of the free electrons. The electric field in this equation is considered as time harmonic with frequency ω. Once the equation is solved, two parts are obtained in the solution. One is transient part and the other is oscillatory part which is in phase with the electric field. Because of the damping factor, the transient part dies with the distance. In our case, the oscillatory part is important. The solution for the oscillatory part can be given as

$$\boldsymbol{x} = \frac{\left(\frac{e}{m}\right)\boldsymbol{E}}{{\omega_o}^2 - \omega^2 - i\gamma\omega} \tag{2.4.2}$$

where ${\omega_0}^2 = K/m$ and $\gamma = b/m$.

By adopting this relation for n oscillators to the constitutive relation for polarization, we obtain

$$\boldsymbol{P} = \frac{{\omega_0}^2}{{\omega_0}^2 - \omega^2 - i\gamma\omega}\varepsilon_0\boldsymbol{E} \tag{2.4.3}$$

where ${\omega_p}^2 = ne^2/(m_e\varepsilon_0)$ and ω_p is the plasma frequency. From equation 2.4.3 the dielectric function of simple harmonic oscillator is derived as

$$\varepsilon = 1 + \chi = 1 + \frac{{\omega_p}^2}{{\omega_0}^2 - \omega^2 - i\gamma\omega} \tag{2.4.4}$$

The real and imaginary parts of it are

$$\varepsilon' = 1 + \frac{{\omega_p}^2({\omega_0}^2 - \omega^2)}{({\omega_0}^2 - \omega^2)^2 + \gamma^2\omega^2} \tag{2.4.5}$$

$$\varepsilon'' = \frac{{\omega_p}^2\gamma\omega}{({\omega_0}^2 - \omega^2)^2 + \gamma^2\omega^2} \tag{2.4.6}$$

Their behavior with frequency is shown in Figure 2.4.2

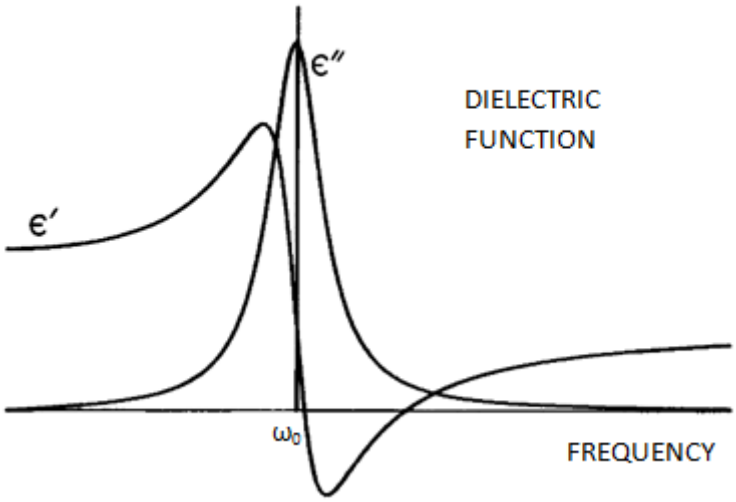

Figure 2.4.2 : Real and imaginary parts of the dielectric function obtained from Lorentz model [36]

2.4.2 Drude Model

The band structure of materials directly affects the optical properties of them. In conductors, a filled band overlaps with an empty band, so there is no threshold energy for an electron to make intraband transitions [42]. On the other hand, the forbidden energy gap in the band structure of a nonconductor requires the supply of energy greater than the band gap for an interband transition. This property explains why the metals are highly absorbing and reflecting, whereas nonconductors are transparent and weakly reflecting for photons with energies less than the band gap.

The electrons in metals at the uppermost energy levels can be excited by photons with very small energies (see Figure 2.4.3).

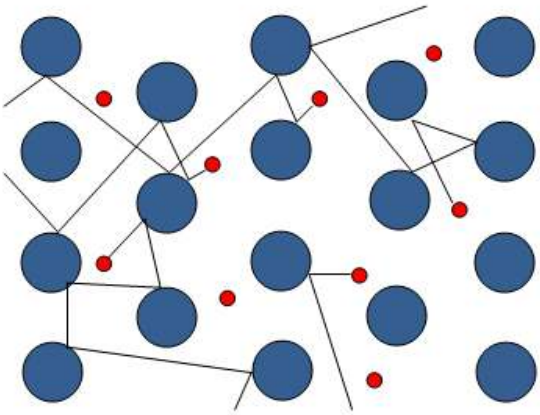

Figure 2.4.3 : Motion of free electrons under an external electric field in Drude model

The optical behavior of these electrons can be analyzed by "clipping the springs" in the Lorentz model, which means that spring constant is set to zero. Then the dielectric function becomes

$$\varepsilon = 1 - \frac{{\omega_p}^2}{\omega^2 + i\gamma\omega} \qquad 2.4.7$$

with real and imaginary parts

$$\varepsilon' = 1 - \frac{{\omega_p}^2}{\omega^2+\gamma^2} \quad , \quad \varepsilon'' = \frac{{\omega_p}^2\gamma}{\omega(\omega^2+\gamma^2)} \qquad 2.4.8$$

Under these circumstances, Lorentz model is converted to the Drude model [36].

In the Drude model it should be paid attention to one point which is the size limit of particles. The damping constant appears in both the Lorentz model and the Drude model as noticed in equations above. The damping constant is directly proportional to mean free path of an electron in the material. As known, the mean free path for metals is in the order of tens of nanometers. Consequently, for a nanoparticle, which has a size comparable with the mean free path length, have a limitation in electron motion. This effect is strongly observable in the Drude model. For this reason, the damping constant is altered as

$$\gamma' = \gamma_{bulk} + \frac{\vartheta_f}{l} \qquad 2.4.9$$

where ϑ_f is the Fermi velocity and l is the effective mean free path affected by the particle boundaries.

Although Drude model seems to be enough for optical characterization of metals, it fails for the higher energy part of the spectrum. High energetic photons tend to promote bound electrons, so they also contribute to the optical behaviors [40]. On the other hand, the Lorentz model only considers the bound electrons. Separately they are not enough to explain the optical properties of real metals. For this reason, a much more accurate result is achieved just by adding the dielectric functions belonging to both free and bound electrons.

$$\varepsilon = \varepsilon_f + \delta\varepsilon_b \qquad 2.4.10$$

The $\delta\epsilon_b$ represents the contribution from Lorentz oscillators and ϵ_f is for the free electron contributions.

$$\varepsilon = 1 - \frac{{\omega_{pe}}^2}{\omega^2 + i\gamma_e\omega} + \sum_j \frac{{\omega_{pj}}^2}{{\omega_j}^2 - \omega^2 - i\gamma_j\omega} \qquad 2.4.11$$

where subscript e is for free electrons.

Up to now, the resonance condition for a particle was considered from both electrostatic approach and Mie theory. The dielectric function, which is the key parameter in determining the resonance condition, was explained by models. When the true model is chosen to solve the dielectric function of the particle, the particle-light interaction would be defined with high accuracy.

2.5 Applications of Plasmonic Oscillations to Photovoltaic Solar Cells

Up to this section, light interaction with a particle and particularly with a spherical metal nanoparticle has been described from a fundamental point of view. In this section, we focus on a particular application of plasmonic system to photovoltaic solar cells. Major issues concerning solar cell applications will be addressed in the light theoretical approaches described in the previous sections.

It is possible to take advantage of metal nanoparticles through two basic mechanisms in solar cells. The first one, which is the dominantly preferred in our experiments, is the light scattering by metal nanoparticles. The second one is the field enhancement in the close vicinity of metal nanoparticles, namely near field effect. In the Figure 2.5.1 below, these two effects are illustrated schematically.

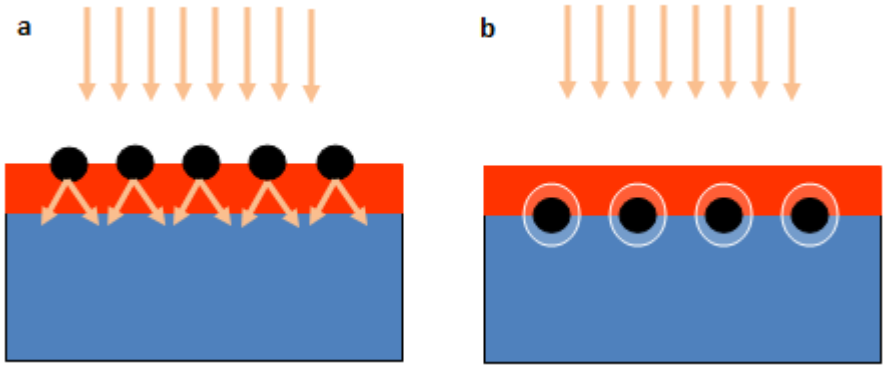

Figure 2.5.1 : Plasmonic light trapping by (a) scattering from metal nanoparticle and (b) excitation of localized surface plasmons in metal nanoparticle

So far, we have discussed the light scattering process by particle in a general case where the nanoparticle and its environment are uniform and ideal. However, the scattering character was not analyzed when the particle is placed near to an interface. A particle embedded in a homogenous medium scatters the incoming light nearly symmetrical into both forward and reverse direction. In many cases, the symmetry is disturbed because the medium around the particle is usually inhomogeneous. Particularly in solar cell applications nanoparticle are placed on a surface, between interfaces of two dielectrics, or in a dielectric with interfaces to the active region of the cell. The light prefers to scatter into the dielectric which has higher permittivity [43]. Actually, this is the point assumed to be an advantage in most of the solar cell applications. The reason of the scattering tendency of the light into the medium with high index is attributed to the high density of optical modes in those mediums.

The light scattered into the medium from metal nanoparticle gets an angular spread. This increases the optical path length in the device. In the case of no metal nanoparticle on the surface, the path length is equal to the thickness of the device. On the other hand, the scattered light from metal nanoparticles which makes an angle to the normal and travels a longer distance in the device as shown in Figure 2.5.2 below. Also, the scattering probability from the backside increases in the case of scattering from the nanoparticles due to the increased angle incidence.

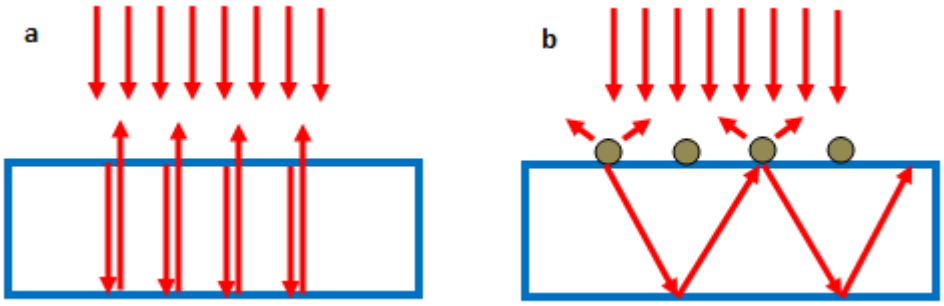

Figure 2.5.2 : Optical path of light without (a) and with (b) metal nanoparticles

In the extreme case in which the light scatters at an angle beyond the critical angle for reflection for the corresponding interface, light is totally trapped in the cell, which corresponds to the most desired situation. For a more detailed analysis, the internal modes should be discussed. The trapped modes and the radiation modes, which are also mentioned as escape cone, cumulatively form the internal modes. The light coupled with radiation modes have more possibility to escape from the substrate without getting trapped inside. On the other hand, the thickness of the substrate directly influences the number of the modes. In Figure 2.5.3 (a) and (b), the mode characteristics are represented for the substrates with a thickness much larger than the incident wavelength and a thickness comparable to the wavelength of the incident light, respectively [44].

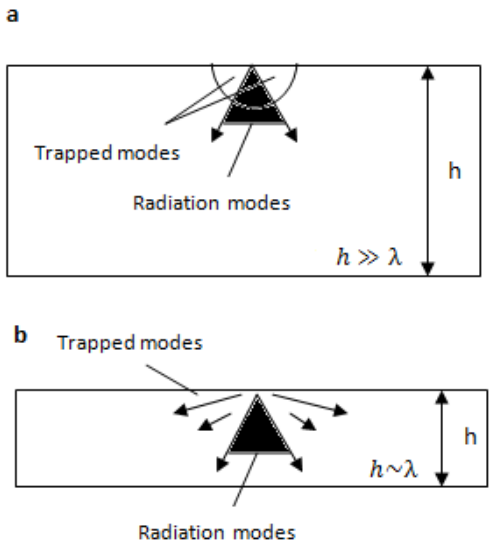

Figure 2.5.3 : Internal modes in substrates when (a) $h \gg \lambda$ and (b) $h \sim \lambda$, where h is the substrate thickness

As can be recognized easily, the light trapping is more limited for thinner substrates, since trapping modes are not continuous as in the case of thicker ones.

Moreover, in order to increase the optical path length, the cell may be coated with a metal back contact. When the light reaches the back contact it is reflected back to the metal nanoparticles and the same scattering mechanism can take place once more.

Rather than the basic properties of light scattering from metal nanoparticles, the coupling efficiency of light into the active region of the device is more important from the device performance point of view. The size and shape of the metal nanoparticle directly influences that efficiency. It is intuitively expected that; the effective dipole moment becomes closer to the interface, and then light will couple more efficiently in the underlying layer. For this reason, cylindrical and hemispherical particles are expected to yield more scattering fractions into the substrate. However, there is a contradiction in size of the particle. Small particles have higher coupling efficiency than larger particles, but very small particles suffer from ohmic losses. When the size is increased to overcome this problem, the scattering rate increases, but at the same time the coupling efficiency decreases.

As mentioned above, plasmonic effect can induce two mechanisms: far- field effect which is the scattering of the light to far regions, and near field effect observed around the metal nanoparticles. In the case of near field effect the incident electromagnetic wave can be coupled into plane waveguide modes in the photoactive material. So, the enhanced localized near field generated around the nanoparticle can excite electron hole pairs in the underlying semiconductor and even without phonon assistance in the indirect band structure. This mechanism increases the light absorption in the photoactive layer per unit thickness. In other words, the nanoparticles in this mechanism act as an effective optical antenna for the incident irradiation. However, this mechanism is efficient for nanoparticles below 20 nm in diameter, since they have lower fraction of light emitted as radiation [43]. These values are hard to achieve using standard fabrication methods.

The far field application depends on the diffusion length of the generated carriers. As the electron-hole pairs are collected around the nanoparticles, their distance to the p-n junction should be smaller than the carrier diffusion length. Otherwise the generated carriers are lost before the p-n junction collects them. In many cases, it is practically not possible to place the nanoparticles in the close vicinity of a p-n junction to make use of the near field effects. Moreover, the absorption rate in the underlying layer has to be larger than the reciprocal of

the plasmon decay time which is in the range of tens of femtoseconds. If this condition is not satisfied, then the absorbed energy is dissipated in the metal nanoparticle as ohmic damping.

For these reasons explained above, in this work, we focused on the light scattering from the metal nanoparticles, which is far field effect of plasmonic oscillations.

2.6 Simulation of the Light Scattering from Metal Nanoparticles

In the first two sections, some theoretical approaches were presented in dealing with the interaction of light with particles which have well defined geometries especially for spherical particles. Although Mie theory can be modified for a couple of geometries, it does not provide an exact solution for particles with arbitrary shapes. There are several numerical methods to overcome the difficulties originating from the particle's shape. The most commonly used ones are the finite element method (FEM), DDA and FDTD.

2.6.1 Finite Difference Time Domain

FDTD is one of the most preferred methods in solving the Maxwell's equations for particles with complex geometries. The method provides a direct time and space solution, thus it becomes preferable in electromagnetics and photonics. Moreover, FDTD serves as frequency solver by applying the Fourier transform and thereby the key parameters like the complex pointing vector, transmission and reflection of light are obtained.

The FDTD method solves curl equations of Maxwell's equations for nonmagnetic materials.

$$\frac{\partial \boldsymbol{D}}{\partial t} = \nabla \times \boldsymbol{H} \tag{2.6.1}$$

$$\frac{\partial \boldsymbol{H}}{\partial t} = -\frac{1}{\mu_0} \nabla \times \boldsymbol{E} \tag{2.6.2}$$

by taking **D** as

$$\boldsymbol{D}(\omega) = \epsilon_0 \epsilon_r{}^*(\omega) \boldsymbol{E}(\omega)$$

where $\epsilon_r{}^*(\omega)$ represents the complex relative dielectric function.

For three dimensional problems, there are six electromagnetic field components in Maxwell's equations. These components are E_x , E_y , E_z , H_x , H_y and H_z . In the case of a system, which is infinite in z direction, the problem is simplified by

$$\epsilon_r{}^*(\omega, x, y, z) = \epsilon_r{}^*(\omega, x, y)$$

$$\frac{\partial \boldsymbol{E}}{\partial z} = \frac{\partial \boldsymbol{H}}{\partial z} = 0 \qquad 2.6.3$$

Under this condition, the Maxwell's equations are divided into two sets of equations which present solutions only in x-y plane. The equation sets are transverse electric (TE) and transverse magnetic (TM) equations. The electromagnetic field components for each set are given below.

$$TE\text{: } E_x \text{ , } E_y \text{ , } H_z$$

$$TM\text{: } H_x \text{ , } H_y\text{, } E_z$$

The TE case simplifies the Maxwell's equations as

$$\frac{\partial D_x}{\partial t} = \frac{\partial H_z}{\partial y} \qquad 2.6.4$$

$$\frac{\partial D_y}{\partial t} = -\frac{\partial H_z}{\partial x} \qquad 2.6.5$$

$$\frac{\partial H_z}{\partial t} = -\frac{1}{\mu_0}\left(\frac{\partial E_y}{\partial x} - \frac{\partial E_x}{\partial y}\right) \qquad 2.6.6$$

Analogically, TM case makes a simplification in Maxwell's equations as

$$\frac{\partial D_z}{\partial t} = \frac{\partial H_y}{\partial x} - \frac{\partial H_x}{\partial y} \qquad 2.6.7$$

$$\frac{\partial H_x}{\partial t} = -\frac{1}{\mu_0}\frac{\partial E_z}{\partial y} \qquad 2.6.8$$

$$\frac{\partial H_y}{\partial t} = \frac{1}{\mu_0}\frac{\partial E_z}{\partial x} \qquad 2.6.9$$

The basic physical background for the FDTD is given above. In this work, the FDTD is used to verify the theoretical expectations and to get an insight for our experimental works. There are several project files which are freely available. To deal with different situations, the

project files should be modified. In our case, the effects of size, shape and dielectric environment of a particle on the resonance condition have been examined by the FDTD technique.

At first, a 3-D Mie theory project file was studied. It gives Mie efficiency for both scattering and absorption processes by comparing the results obtained from FDTD and Mie theory. However, the increase in the background index simultaneously disturbs the coherence between simulation and the Mie theory. In Figure 2.6.1 and Figure 2.6.2, the Mie efficiency for scattering and absorption cross section for a spherical particle with 40 nm radius in air is presented, respectively. X-axis is indicated as size parameter, which is $x = ka$ as given previously.

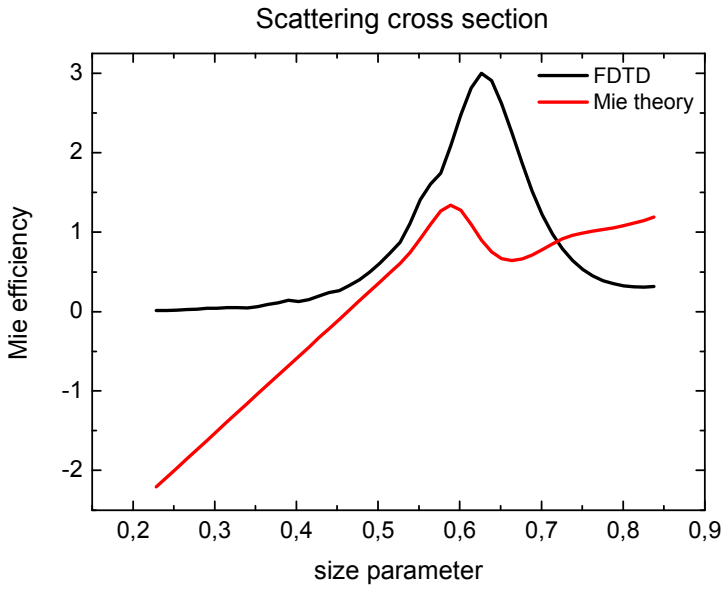

Figure 2.6.1 : Scattering cross section of a spherical particle with 40 nm radius in air

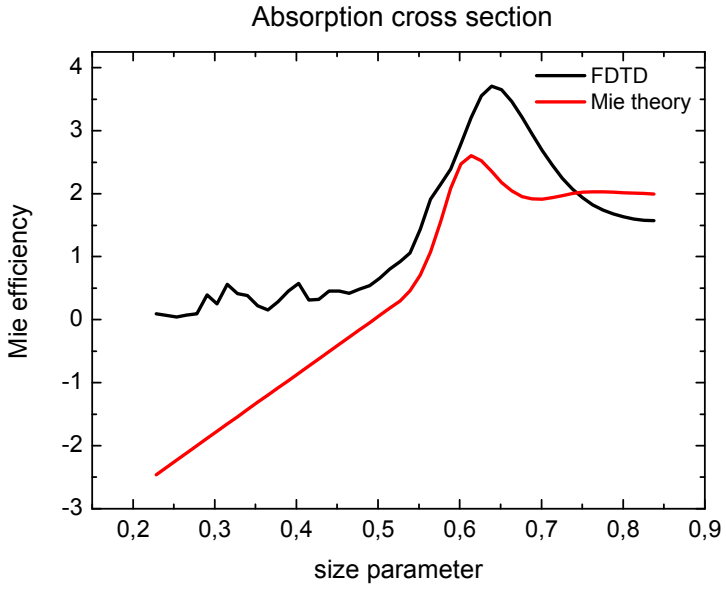

Figure 2.6.2 : Absorption cross section of a spherical particle with 40 nm radius in air

Just by changing the background index to 1.5, which can be attributed to embedding the particle in glass, the graphs below were obtained (see Figure 2.6.3 and Figure 2.6.4). Although the behavior of Mie theory does not change, the result from FDTD changed significantly.

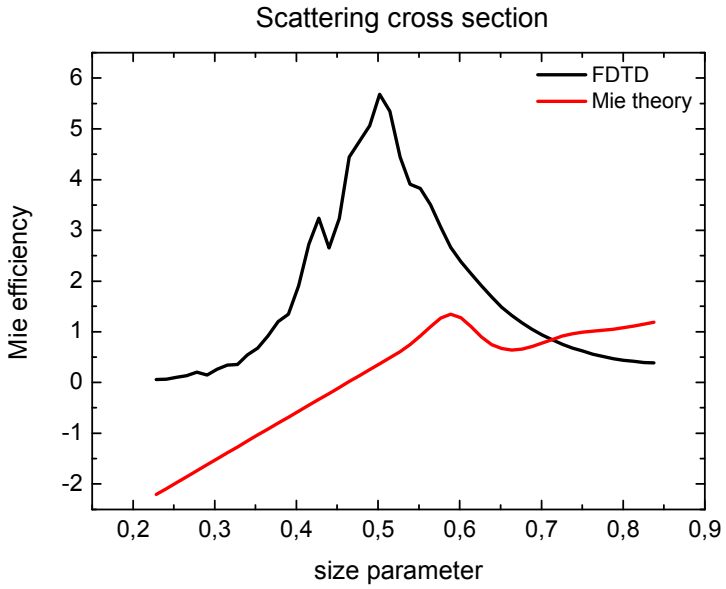

Figure 2.6**.3 : Scattering cross section of a spherical particle with 40 nm radius in a medium with 1.5 refractive index**

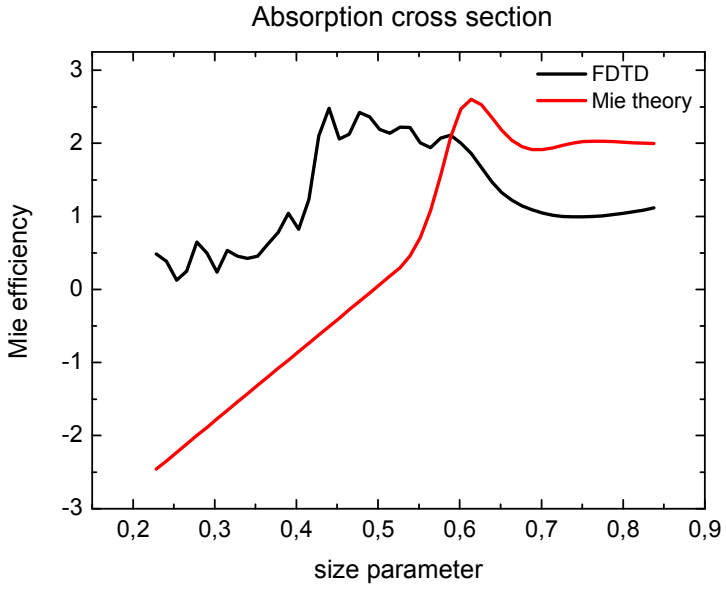

Figure 2.6.4 : Absorption cross section of a spherical particle with 40 nm radius in a medium with 1.5 refractive index

In another project file, the size effect was considered by simulating the particle cross sections in 2-D. The radius of the particle was changed from 20 nm to 40 nm by keeping the other parameters same.

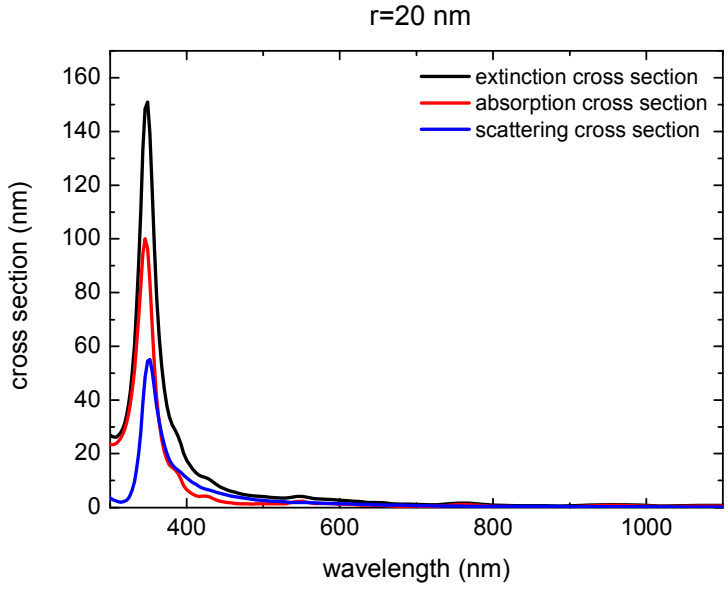

Figure 2.6**.5 : Cross sections of a spherical particle with 20 nm radius in air**

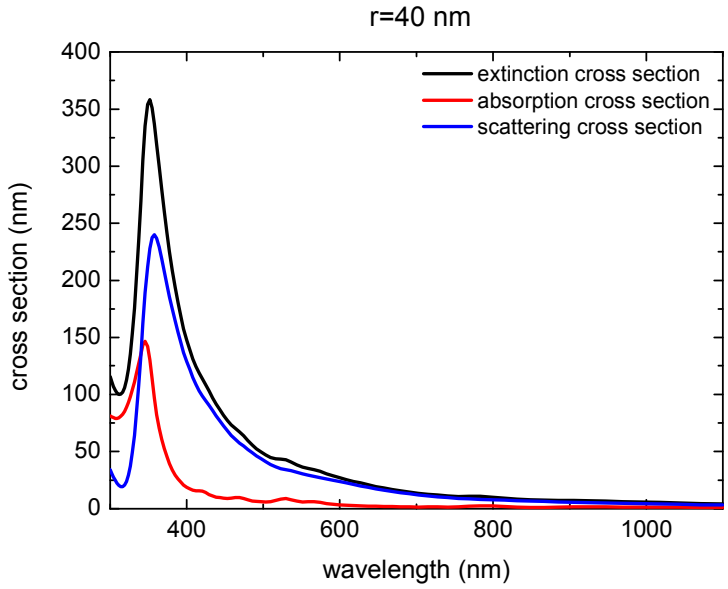

Figure 2.6.6 : Cross sections of a spherical particle with 40 nm radius in air

From Figure 2.6.5 and Figure 2.6.6, it is easily concluded that absorption is more dominant than scattering for small particles, which was commented from the cross sections obtained from electrostatic approach in the preceding section. Moreover, the redshift of cross sections with increase in size are consistent with the theoretical expectations. Another effect, which was taken into account during the simulation study, is the orientation of the nonspherical particles. When an ellipsoidal particle is oriented in two different ways, the cross sections are obtained as shown in Figure 2.6.2 and Figure 2.6.8. The particle is illuminated in the forward direction along the y-axis with TE polarization.

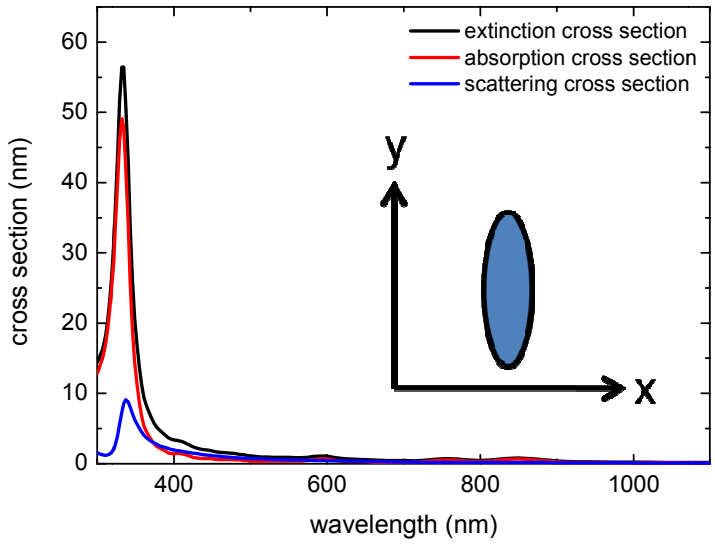

Figure 2.6.7 : Cross sections of an ellipsoidal particle with 10 nm minor axis and 40 nm major axis in air in the case of the major axis is in the y-axis

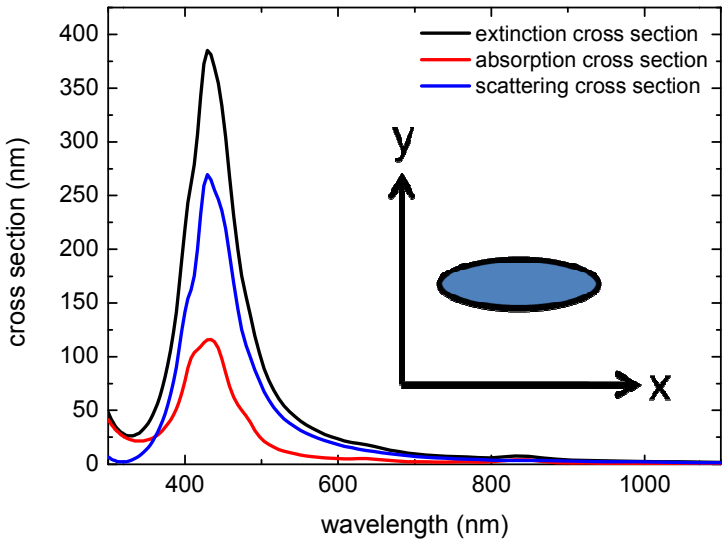

Figure 2.6.8 : Cross sections of an ellipsoidal particle with 10 nm minor axis and 40 nm major axis in air in the case of the major axis is in the x-axis

For the first orientation shown in Figure 2.6.7, the minority axis dominated the cross section character for the TE polarization. When the particle is rotated by 90°, the resonance peak for the cross sections redshifts since the majority axis becomes effective in this case.

In order to observe the plasmonic behavior in our samples, backward scattering measurement, which is introduced in the third chapter in a detailed way, was conducted. For this reason, the project file, which generates the reflection character of a particle under the specified condition, was taken into the consideration. The same system was put into simulation just by changing the background index. The reflection from a particle with 40 nm radius in both $n = 1$ and $n = 1.5$ was simulated (see Figure 2.6.9 and Figure 2.6.10).

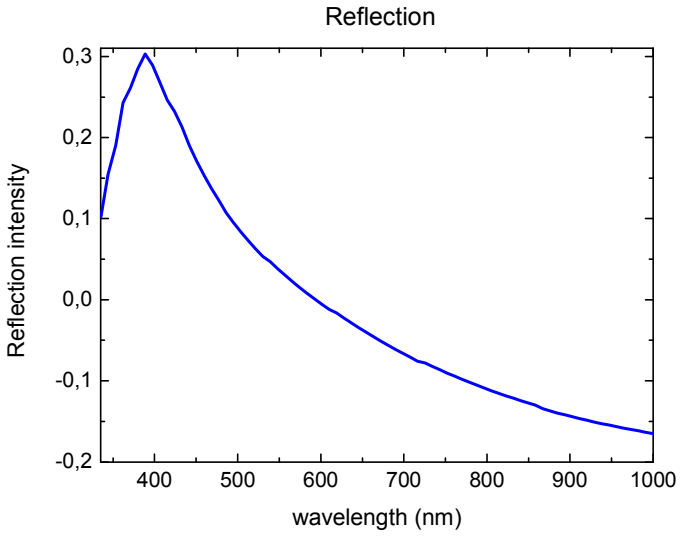

Figure 2.6.9 : Reflection from a spherical particle with 40 nm radius in air

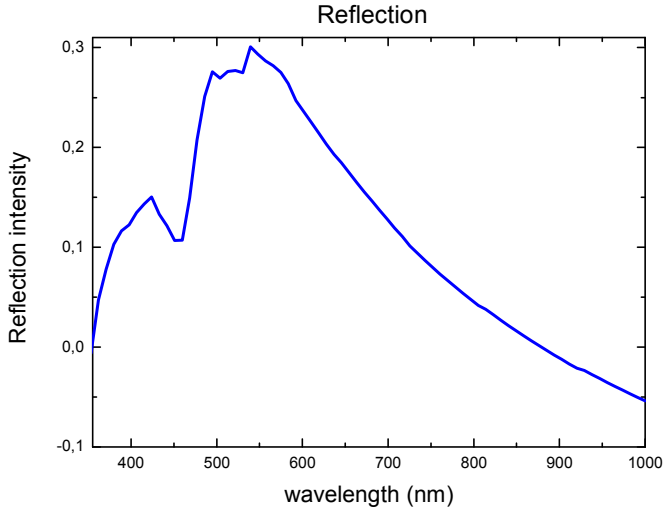

Figure 2.6.10 : Reflection from a spherical particle with 40 nm radius in a medium with 1.5 refractive index

For the particle in a medium with higher index, there are two points which should be discussed. The first one is the redshift with the increase in the index of the medium. The physical background of this case was considered during the electrostatic approach in particle-light interaction. The second point is the extra peak emerged in the graph for the particle in a medium with $n = 1.5$. This peak can be attributed to multipole peak. The electrostatic approach is not an accurate way for the analysis of higher order modes. Moreover, the Mie theory approach does not have a straight forward solution, so performing numerical simulation based on the Mie theory is more practical. The modifications in the project file provide to complement the theoretical expectations with simulation. However, for the fabricated nanoparticles it is quite hard to define a compact case for simulation. The boundary conditions, which are significant for considering the interaction between two particles, are totally different for any region on substrate. On the other hand, the local dielectric environment of the particle is not homogenous because of the inhomogeneity in the contact areas of the particle. Because of all these drawbacks, it is hard to complement the experimental results to the simulation directly.

CHAPTER 3

EXPERIMENTAL TECHNIQUES

3.1 Fabrication Methods

In this chapter, we summarize the experimental techniques, procedures and conditions used during this study. During the course of this thesis work, we have applied many of the material and device processing and characterization techniques. EBL, thin film formation with vacuum deposition, annealing, oxidation, nitride formation, and optical characterization are extensively used in many experiments. Some of these techniques are well known and their descriptions are widely available in the relevant textbooks. For this reason, we avoided giving detailed description of the equipment systems unless there is some specific feature which is particularly important for the presented work.

3.1.1 Electron Beam Lithography

EBL is the first method which was chosen to fabricate metal nanoparticles in this study. It is one of the most preferred fabrication methods for well-defined patterns on a substrate. The term well defined means for EBL is because it produces particles with controllable size and shape. EBL is a sensitive and multi-step process which needs extreme care and long durations. It is not suitable for surfaces with large area. For these reasons, the EBL is not an appropriate fabrication technique for large scale industrial production.

The EBL that is used in this work is based on a Cam Scan CS3200 SEM to which a laser interferometric stage fabricated by the company Softsim and a pattern generator of Xenos are installed. The system operates under high vacuum, usually less than 10^{-5} Torr. The filament in our system is a tungsten filament generating an exposure current at 2.30 A for 20 kV. In this study, ITO coated microscope slides with surface resistivity of 70-100 Ω/sq and transmittance of >87% were used as substrate. The thickness of the ITO coating was 15-30 nm. Since ITO is a conductive layer, it mostly prevents the charging effect. Before starting the process substrates were cleaned in an ultrasonic bath with acetone, isopropyl alcohol (IPA) and deionized (DI) water. For the lithography process with the electron beam exposure, the substrate is coated with an electron beam resist. The resist materials are classified as positive and negative resist depending on their reaction to the exposure of the light. The exposed area is decayed for positive resist and the unexposed area for negative resist. In our case we used a positive resist for the EBL process.

The C2 950 Poly (methyl methacrylate) (PMMA), which is the product of MicroChem, was chosen as the resist material. Following the specifications given at the website of MicroChem, the substrate was coated with 100 nm PMMA at 6000 rpm. After the coating, the sample was baked at 170 °C for 30 minutes and prepared for exposure.

For the production of nanoparticles, disk shaped patterns were chosen at first, because of their simplicity. To be able to decrease the size of disks, dots are preferred rather than full circles in order to minimize the proximity effect. There are several key parameters to control the size and the geometry of the particles such as; dwell time, dose of exposure, field size and current during the exposure.

For a successful operation of the EBL system, the following steps should be carried out very carefully: proper beam alignment, aperture selection, focus-astigmatism tuning and stabilizing the beam current. If these steps are misconducted, then the pattern may not be exposed or unexpected geometries may be obtained. The Figure 3.1.1 below clearly shows the problem caused by astigmatism.

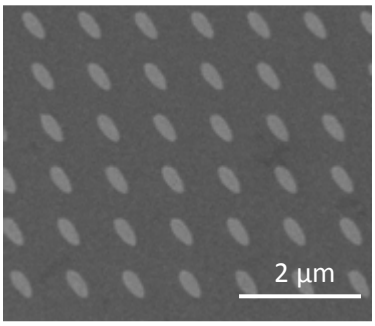

Figure 3.1**.1 : Astigmatism problem observed in a sample produced by EBL**

The dwell time and the dose of exposure are directly proportional to the charge deposited into the resist. Thus, these parameters directly affect the increase in size by the proximity effect. But still there are some other dynamics to be taken under control. To conserve the symmetry of the geometries and obtain high resolution, the dwell time should be high and the field size should be small. Moreover, to hasten the lithography process the dose of the exposure and the current may be increased, but the minimum disk size becomes limited as a drawback of this procedure.

After having completed the pattern exposure, the sample should be developed by methyl isobutyl ketone (MIBK): IPA 1:2 in volume for 70 seconds, and a dip in IPA for 30 seconds and finally rinsed by DI water. This final step was done to remove the residues of the PMMA at the exposed regions. A 12 nm Au film was evaporated on to the patterned surface in the e-beam evaporator chamber at $3\text{-}5\text{x}10^{-6}$ Torr. The metal film coating process is explained in the following section.

Finally, the lift off process should be done to obtain Au nanoparticles. Acetone was used as chemical for this step, it penetrates under the evaporated Au film and removes PMMA from the unexposed area, leaving the Au nanoparticles on the surface. After several recovery trials, we found that the lift off process is faster on a hot plate. In Figure 3.1.2 below, all steps of an EBL process are summarized.

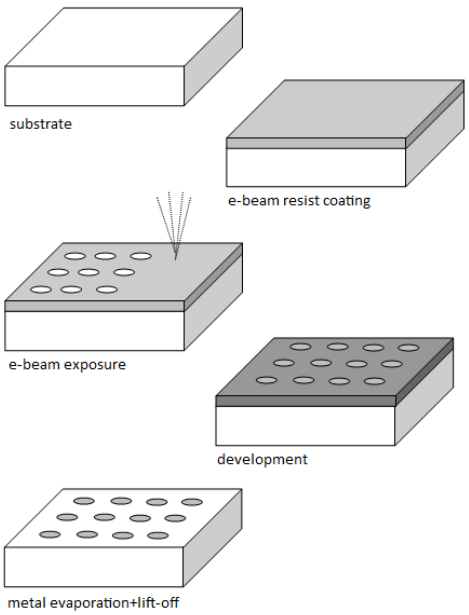

Figure 3.1.2 : Steps followed in EBL fabrication method

Figure 3.1.3 shows an SEM image of the sample with Au nanoparticles prepared by the lithography process explained above.

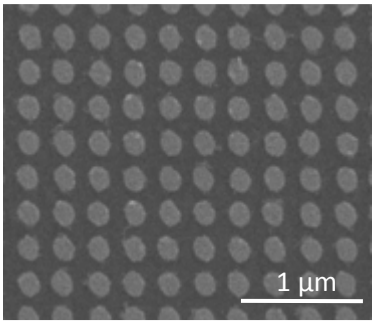

Figure 3.1.3 : Au nanoparticles after completing the whole steps in EBL fabrication

3.1.2 Dewetting

As mentioned in the previous chapter, the EBL is not a proper fabrication method for large-scale applications that are necessary for solar industry. For this reason alternative fabrication methods should be developed. The fabrication of metal nanoparticles by the so-called thin film dewetting is the most suitable fabrication method of metal nanoparticles for large area

applications. The fabrication process is quite easy and straightforward. However, there are several parameters that have to be optimized.

In this work, substrates listed in Table 3.1.1 were chosen to test the effect of substrates on the plasmonic effects.

Table 3.1.1 : List of substrates used in dewetting methods

Si ((100) oriented, 4″ single crystal Si wafers with 5-10Ω-cm B)
Si + Si_3N_4
Si + SiO_2
Glass + ITO
Surface textured Si
Surface textured Si + Si_3N_4

The same cleaning procedure was applied to all substrates. At first, the sample was put in the ultrasonic bath with acetone. Since the acetone is a very good solvent, it dissolves the organic compounds. Then, the substrate was put in IPA especially to dissolve again some organic contamination. Finally, the sample was rinsed with DI water. For the Si based substrates, after the standard cleaning process the natural oxide layer on the Si was removed by dipping the wafer into a hydrofluoric acid (HF):DI water solution with a proportion of 1:20.

In each set of samples, we aimed to observe the effect of different substrates and dielectric layers. SiO_2, Si_3N_4 were used as dielectric layers in this work, since these are the standard materials for solar cell applications. There are two choices for oxidation processes, dry oxidation and wet oxidation. However, the thickness of the oxide layer can be more accurately controlled by dry oxidation. For this reason, dry oxidation was preferred in this work. The oxidation process was carried out in the oxidation furnace, which is used for a standard solar cell production. For Si_3N_4 deposition, a Plasma Enhanced Chemical Vapor Deposition system (PECVD) was used. In this process, Si_3N_4 formation takes place through decomposition of silane (SiH_4) and ammonia (NH_3) gases at 380 °C in plasma. The plasma is obtained by radio frequency (RF) source with 50 kHz frequency. The Si_3N_4 deposition process is illustrated in Figure 3.1.4;

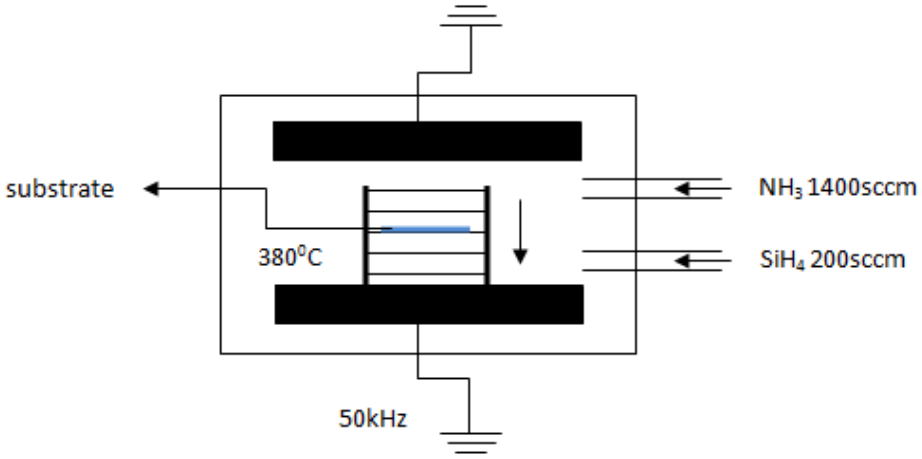

Figure 3.1.4 : Schematic representation of PECVD for Si_3N_4 deposition

The chemical processes for SiO_2 and Si_3N_4 are represented in below, respectively.

$$Si + O_2 \rightarrow SiO_2$$

$$3SiH_4 + 4NH_3 \rightarrow Si_3N_4 + 24H_2$$

After the process, the thickness of SiO_2 layer was measured by the ellipsometer and the Si_3N_4 layer thickness was determined from the color chart.

Metal nanoparticles were fabricated using, Au and Ag metal film which was coated by thermal evaporation in a vacuum chamber under a base pressure of 2-4x10^{-6}Torr. One of the most critical parameters in the study is the film thickness. The thickness of the film was controlled by thickness monitor. From the earlier studies of our research group and the experiences we obtained, the thickness of the metal film was taken to be 12 nm which is known to generate metal nanoparticles with the desired dimensions. After the thin film formation, the samples were annealed in a tube furnace under N_2 with the flow rate 150 sccm in order to induce the formation of metal nanoparticles on the surface of the substrate. In the annealing step, there are two parameters to optimize: annealing temperature and duration.

There are several theoretical approaches for the explanation of the metal nanoparticle formation. One of the most widely accepted approach is based on the phenomenon called thin film dewetting. This dewetting process is based on the capillary instability, which is driven by surface energy minimization which was first studied by Lord Rayleigh [45]. Thin films with a thickness less than 100 nm are exposed to capillary instability because of their high surface to volume ratio [46].

Rayleigh considered an infinite liquid cylinder with radius R during his theoretical analysis and found that the cylinder is unstable to small perturbations with dimension λ which is greater than 2πR. After this perturbation the cylinder decomposes into liquid droplets. When Nichols and Mullins applied a similar theoretical approach to solid cylinder, they found the same results as Rayleigh [47]. The only difference was that the decomposition process is not governed by hydrodynamics for solid cylinder. However, the perturbations considered above are not enough to decompose a thin film. The film decomposes into particles only when the perturbation can penetrate the film [48].

For a solid and defect free film, a mechanism starts at the boundary of the film by a surface energy gradient because of the edge agglomeration driven by capillary instability and it is followed by the particle formation via Rayleigh instability. Actually this is the ideal case, since almost all the real films have defects and inhomogeneity in the film thickness. The tendency of the minimization of interfacial energy with the contributions of defects causes grooves in the film. These grooves can reach the substrate and form stable voids. The material in the film is transferred to the periphery of the hole by a self diffusion. The growth of voids causes edge agglomeration and as a result thickened edge [49]. Rayleigh instability due to the material accumulations causes inhomogeneity in the film thickness. Jiran and Thompson stated that the voids penetrate faster in thinner regions of the film with a growth rate proportional to h^{-3} where h is the film thickness [46]. As a result, the film decomposes into individual islands. Since the annealing promotes the atomic diffusion, dewetting process takes place in a moderate time. This description of thin film dewetting can be applied to many practical applications under certain conditions. However, dewetting is quite complicated for metal film during long time annealing. In this case, the metal-surface interactions should be considered [50]. Long time dewetting process is still under debate.

As widely discussed in the literature, following the dewetting process a hillock growth is commonly observed [51, 52]. There have been several approaches to explain the hillock growth. It was attributed to the stress relaxation [53], surface diffusion [54], and lateral diffusion caused by the stress gradient [55]. From an overall and a general point of view, the metal nanoparticle formation can also be explained by the difference in the thermal expansion coefficients between metals and the substrates which were used in this work. Since the stress distribution is inhomogeneous through the metal film and the substrate, a stress gradient is formed. As a consequence, the film migrates from the stressed region to relaxed region as a hillock. Through this surface diffusion, holes are formed on the surface.

By changing the thickness of the film, annealing temperature and duration, the sizes and distribution of hillocks are controlled. Since, in this work, the thickness of film is relatively thinner than the thicknesses reported in the literature; the hillocks are in the form of spherical or hemispherical nanoparticles. Moreover, the thinner film requires lower annealing temperature for the formation of nanoparticles.

3.1.3 Image Analysis

The samples with metal nanoparticles were imaged with QUANTA 400F Field Emission SEM at the Central Laboratory of METU. The imaging is the key step for both qualitative and quantitative analysis for each set of samples. Quantitatively, it provides to check whether the particles have formed or not and have an idea on the shape of the particles. For a deeper qualitative analysis, the SEM images were processed with an image analysis program called Gwyddion.

If the image is noisy, it can be filtered at first. The primary aim of the program is to form a mask which covers only the particles. Depending on the need in the analysis, particles below a threshold value can be excluded. In Figure 3.1.5, a masked image is shown.

Figure 3.1.5 : A representative SEM image after masking the nanoparticles

The region colored with red is the mask generated by the program. The importance of the mask is that the analysis only considers the region under the mask. In order to be consistent and minimize the error in the analysis, the images taken under same magnification for each sample in a given set were analyzed.

Throughout the analysis, we were mainly interested in some of the outputs of the analysis program. The grain statistics give information about the number of particles, their projected area both in absolute values and relative values, mean particle size and area. In order to observe the size distribution, the statistics of the equivalent disc radius was plotted for each sample. The graph shows the disc radii with their populations. An example for this kind of graph showing the statistics of the disc radii is given below, in Figure 3.1.6.

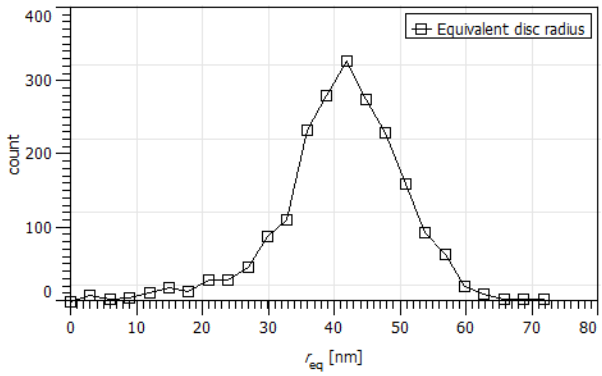

Figure 3.1.6 : An example for an output of equivalent disc radius

Image analysis enables us to make comments on the effect of substrate and annealing temperature on the formation of particles. The outcomes of this analysis are used in the simulations of plasmonic oscillations.

At this point, we should mention that this dimensional analysis should be carried out for many samples to accumulate reliable data for an accurate investigation. However, the analysis method presented here provides fairly reliable results to reach some basic conclusions.

3.2 Characterization

The plasmonic responses of the samples can be observed from the scattering measurements. The peak position corresponds to the resonance condition. The photograph of the optical setup is shown below [Figure 3.2.1].

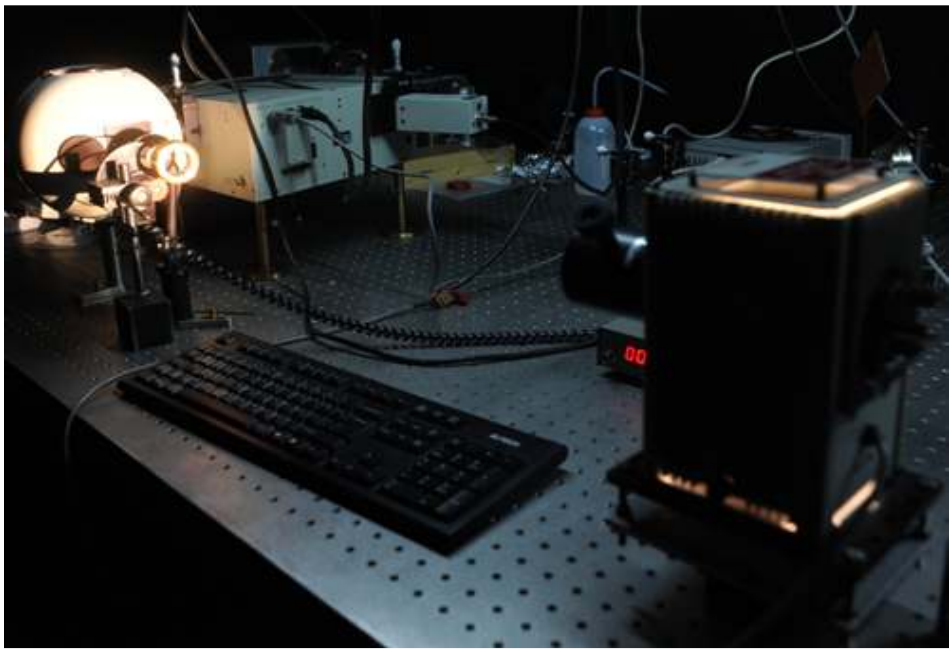

Figure 3.2.1 : Photograph of optical setup

A schematic diagram is given in Figure 3.2.2 for easy identification of each element in the setup and to describe their functions during the measurements.

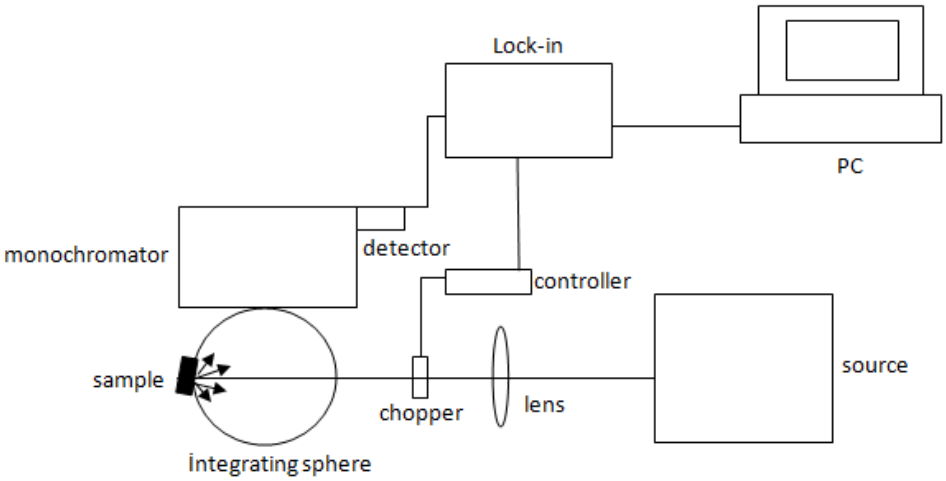

Figure 3.2.2 : Schematic diagram of optical setup

The light source is a halogen lamp and during the measurements its power was set to 99 Watts. Then the incoming light is focused through a lens. The light is modulated by a chopper whose frequency can be varied. The modulated signal at the controller connected to the chopper should be the same value as the signal reached at lock-in amplifier. During the

data acquisition, the sensitivity should be carefully set to a range in order not to cause an overload in the signal.

The most critical element included by setup is the integrating sphere of the Oriel. The sample is placed to the holder with 4° tilt. For reflection measurements the holder is placed as shown in the Figure 3.2.2, to the back of the sphere and for transmission measurements to the front side. The reflected beam in the sphere arrives at the monochromator. The Oriel Si detector is connected to the output of the monochromator and the signal is amplified by the lock-in amplifier of Stanford Instruments. At the end, the data reaches the computer through a program written in LabVIEW, which also includes several controls for the measurement such as; the sensitivity of the measurement, the period of taking each data and the wavelength range of the measurement.

The key function of the integrating sphere is to include the diffused light in the measurement [Figure 3.2.3]. Since the nanoparticles diffuse the incident light in all directions, the measurement with integrating sphere gives more accurate results. Furthermore, a baffle may be included to the system to eliminate the specular reflectance from overall reflectance.

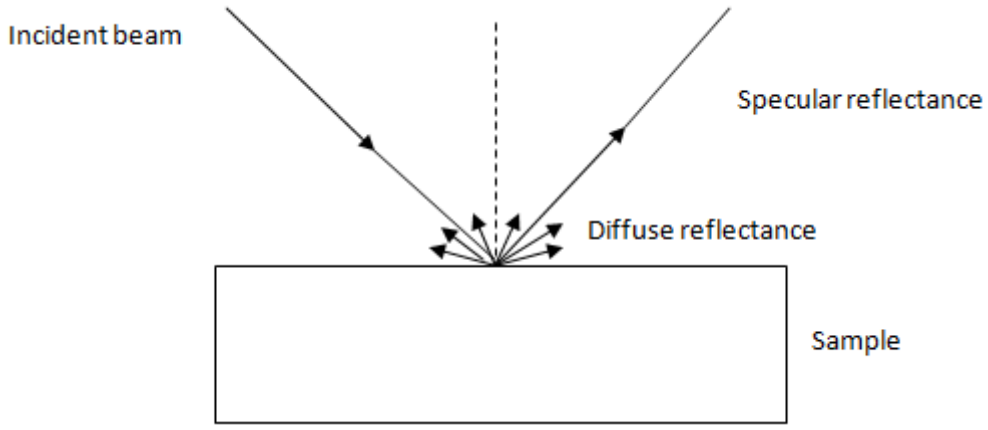

Figure 3.2.3 : Reflection from a nanoparticle

The measured data should be corrected with dark and calibration disk measurements. The dark measurement is taken without any element at the holder and the calibration disk is assumed to have 100% reflectivity. Thus, the dark data is subtracted from both measured and calibration disk data in order to remove the contribution from the ambient. Then the measured data from the sample is normalized with the calibration disk data as given below.

$$I_{normalized} = \frac{I_{measurement} - I_{dark}}{I_{reference} - I_{dark}}$$

For the Si based sample the transmission measurements were not made since they had 525 μm thickness. On the other hand, it is possible to conduct transmission measurements for ITO coated glass based samples. By assembling reflectance and transmission data, the absorption of the nanoparticles can easily be evaluated from the relation

$$I_{absorption} = 1 - I_{transmission} - I_{reflection}$$

The optical characterization setup is the very crucial in the evaluation of plasmonic behavior of the fabricated samples as we observe the resonance conditions as a peak in the scattering spectrum. The nanoparticles basically absorb and scatter in both forward and reverse directions. Throughout the measurements, the information about the backward scattering process is obtained.

To observe the relative changes in the samples after any processes that metal nanoparticle go through, the samples are characterized optically before and after the process. In this way, the effects of that particular process and substrate and the metal type can be extracted from the scattering measurements. The measurements were analyzed and discussed in the results and discussion part.

CHAPTER 4

RESULTS AND DISCUSSION

4.1 Formation of Metal Nanoparticles by EBL

4.1.1 Exposure and Shape of the Dots

The fabrication of metal nanoparticles by EBL is a delicate process which needs special attention. The most crucial step is the exposure of the pattern at the beginning. The calibration of the EBL system should be done carefully to obtain stable and well defined beam spot. Due to fluctuations in current density and exposed area, it is hard to obtain the designed pattern. In order to avoid shape deformation, the astigmatism originated from the electron beam lens system should be corrected. However, sometimes the astigmatism control can be turned off deliberately in order to obtain particles with ellipsoidal shapes.

In this work, the EBL patterns were created using dot and circle geometry on ITO coated glass substrates. For simplicity, first patterns were created with a period of 5 μm between the particles with a beam current of 175 pA. This large distance was chosen to prevent the possible merging of neighboring dots, since at the beginning it was hard to predict the exact dimensions of the dots for a given set of beam parameters. To observe the effect of dwell time on the size of the dots, different dwell time values were chosen for different sample set. As can be seen in the SEM images in Figure 4.1.1, the dwell time increases the exposure dose.

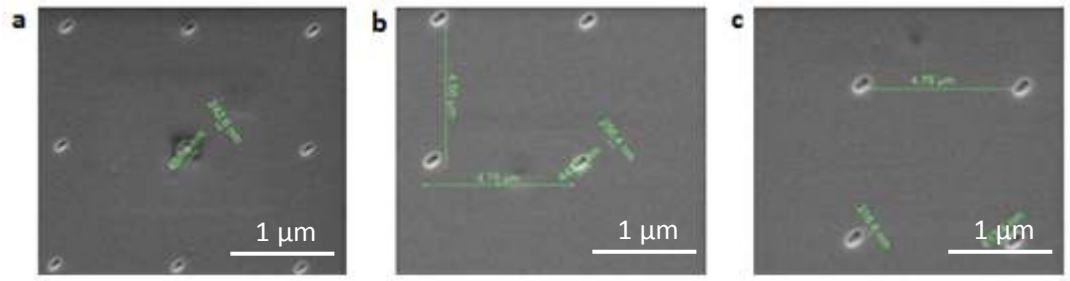

Figure 4.1.1 : SEM images of patterns exposed with dwell times of 1000 µs (a), 4000 µs (b) and 5000 µs (c)

The doses on each dot in the corresponding arrays are 175 fC, 700 fC and 875 fC, respectively. As it is seen from the SEM images, we obtained larger dots for longer dwell times. The dots' shape is ellipsoidal in these samples because the astigmatism was not corrected. The aspect ratio is almost the same for all arrays. Although the shapes of the dots are deformed due to the astigmatism, their period could be controlled precisely because the accuracy of the stage motion is independently controlled by a sensitive interferometer.

In the second set of samples, the period of the dots was decreased to 1µm and the beam current was increased to 230 pA. The higher beam current deposited higher doses into the sample for a given dwell time than the previous samples. This resulted in a larger dot size with higher aspect ratio. The SEM image of the array, whose dwell time is 2250 µs and dose of 517.5 fC, is given in Figure 4.1.2 below.

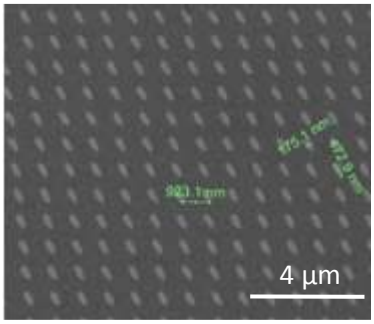

Figure 4.1.2 : SEM image of the dot array exposed with dwell time of 2250 µs

In another attempt, the patterns were created with circles (rather than dots defined by the e-beam spot) whose diameters were 100 nm and period between circles was 300 nm. The total field size was again 100 µm. The beam current was set to 225 pA, almost the same as the previous set of pattern. The SEM images of the arrays exposed with dwell times of 300 ns

and 400 ns are given below. It is seen that more circular geometry was obtained when circles, which were defined previously by the software, was used. With the new pattern dimensions and shorter dwell times we approach the intended shape.

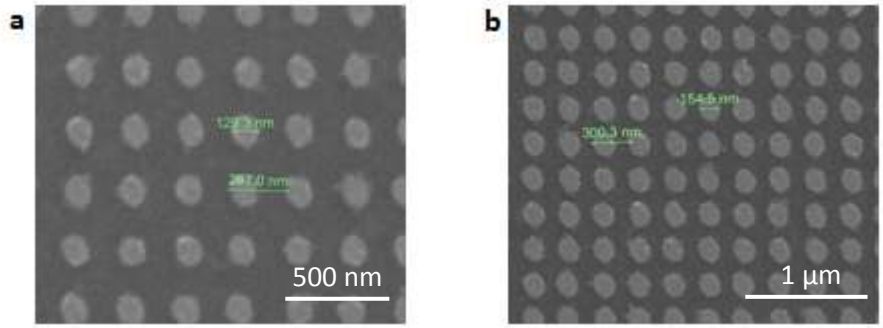

Figure 4.1.3 : SEM image of the circle arrays exposed with dwell times of 300 ns (a) and 400 ns (b)

The effect of dwell time can be seen from Figure 4.1.3. Here, we used two different dwell times for the same geometry. Again the period of the particles are almost under control. However, the dimension of the circles exceeded in larger fractions as the dwell time increased. The dose on the circles increases from 250 $\mu C/cm^2$ to approximately 1170 $\mu C/cm^2$.

4.1.2 Metal Nanoparticle Formation

In the previous section, we discussed the problems faced during the exposure and beam adjustment. Here, a short description and discussion of metal lift-off process is given. As described in Chapter 3, the metal film is evaporated on the PMMA film with the pattern defined by the EBL exposure. Following the metal thin film coating, the metal on the unexposed regions should be removed to obtain the pattern. For this purpose, the sample is rinsed with acetone which attacks the PMMA film under the metal layer.

The lift-off process is a very sensitive to many sample and process parameters like film thickness, process temperature, ultrasonic agitation etc. In many cases, we failed to obtain a well defined pattern. One such example is shown in Figure 4.1.4, where the lifted part of the film re-stuck to surface following lift off. After many attempts, we have obtained optimum process conditions with lift-off process by a heat treatment process on a hot plate.

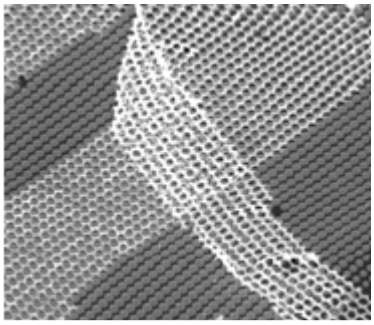
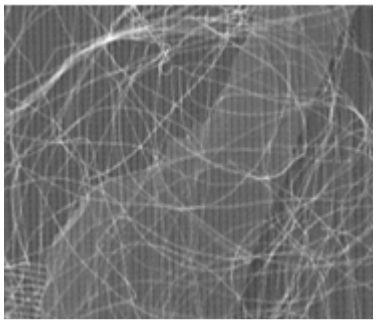

Figure 4.1.4 : SEM images of samples which were unsuccessful after lift-off process

Following the optimization of the parameters such as dwell time, beam current, dose on, film thickness, lift-off, it is quite straightforward to fabricate any pattern needed. However, the standardized parameters changes for various substrates. We should note that the optimization study should be repeated for each metal and substrate system. This requires very long and tedious experimentation. In addition, although EBL provides well defined fabrications, it is not a proper technique for the mass production. For these reasons, we studied the alternative technique in the rest of this work, namely dewetting of thin metal film for the metal nanoparticle formation on large area.

4.2 Formation of Au and Ag Nanoparticles by Dewetting Technique

As it was mentioned in the second chapter, the material of the nanoparticle is quite important in plasmonic behavior as well as the surrounding medium. There are a couple of metals which have attracted attention because of their superior optical properties. Before giving the details about the properties of these metals, let us remember the theory of metal nanoparticles in an electromagnetic field. When only the metals are considered, Drude model is enough for the dielectric function definition. By substituting the dielectric function expansion, which is derived for the Drude model (see Chapter 2), into the polarizability term derived from electrostatic formalism, the polarizability turns out to be

$$\alpha(\omega) = 4\pi\varepsilon_0 a^3 \frac{{\omega_p}^2}{{\omega_p}^2 - 3\omega^2 - i\gamma\omega} \qquad 4.2.1$$

The surface plasmon resonance frequency is then obtained from $\omega_{sp} = \frac{\omega_p}{\sqrt{3}}$. From the expansion of plasma frequency given before (see Section 2.4.1), it is not hard to make a comment on metal selection. Aluminum and Ag have higher free electron density than copper and Au. For this reason, aluminum and Ag have surface plasmon resonance in UV region and the others have in the visible range. This; however, is based on assuming a large particle size. As we discussed in Chapter 2, the resonance frequency can be tuned by the size and the shape of the particle and also by the surrounding medium.

Ag and Au have similar values for the real part of the dielectric functions. However, the imaginary parts of their dielectric functions, which determine the absorption properties, are quite different. This explains why Au has higher absorption coefficient than Ag. For the solar cell or photo detector applications, the scattering is much more important than the absorption. For this reason, Ag has been the most attractive metal for plasmonic applications. However, Ag nanoparticles suffer from the oxidation and sulfidation when exposed to air. This causes variation in their optical behavior. Just to mention, although copper is cheap and readily available, but it is not considered for this application due to its high absorbance. In this study, in order to avoid the instability caused by the sulfidation and/or oxidation, we chose Au as the starting material for nanoparticle fabrication in spite of its optical disadvantages in comparison with Ag. For this purpose, the (100) oriented Si wafer was coated with 12 nm Au film by thermal evaporation. After cutting them into small pieces, some parts were annealed at 300 °C, 400 °C and 500 °C for several durations, separately in a furnace under N_2 flow. The SEM images shown in Figure 4.2.1 and Figure 4.2.2 below were taken from these samples.

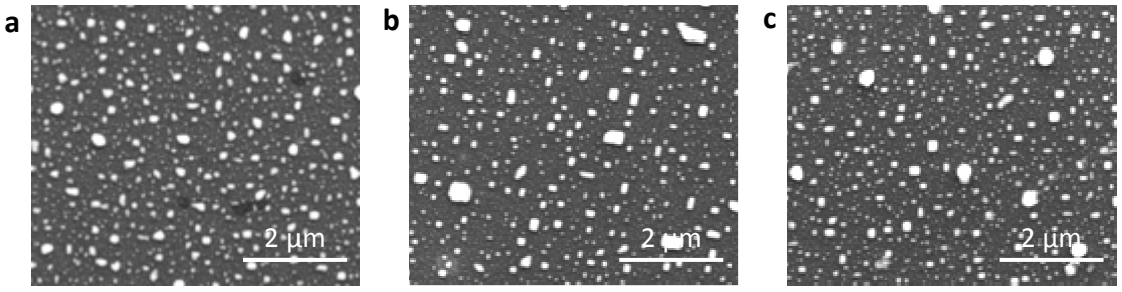

Figure 4.2.1 : SEM images of Si (100) wafers coated with 12 nm Au film which were annealed at 300 °C (a), 400 °C (b) and 500 °C (c) for an hour

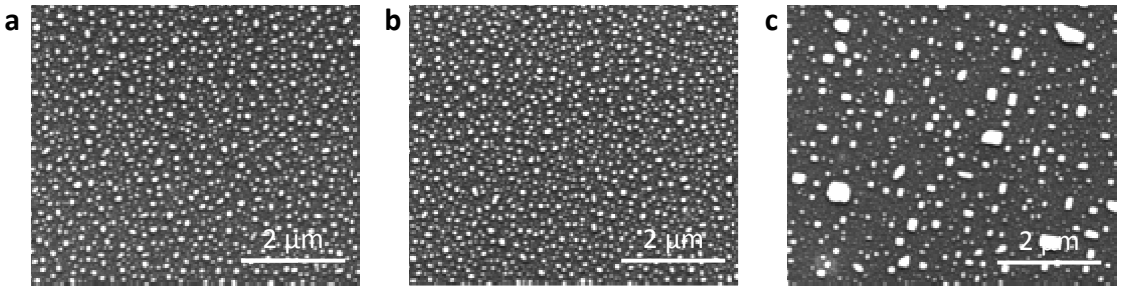

Figure 4.2.2 : SEM images of Si (100) wafers coated with 12 nm Au film which were annealed at 400 °C for 5 minutes (a), 15 minutes (b) and one hour (c)

The reason for annealing the samples at 400 °C for 5 and 15 minutes is to observe the effect of annealing durations on particle formation. From this experiment, we observed that the sizes of the particles are severely inhomogeneous, particularly in the samples annealed at high temperatures. Although not very reliable due to the inhomogeneity, we attempted to obtain the mean particle size from these images. The mean particle size of the samples annealed for 1 hour was found to be 54 nm with FWHM of 16 nm, while it is 51 nm with FWHM of 8 nm for the samples annealed for 5 and 15 minutes. We found that the particle size is more sensitive to annealing duration than annealing temperature. This is showing that the particle formation process is a time limiting process and does not depend on the temperature. Moreover, it is commonly observed that Au film tends to crystallize and their shapes take the form of crystalline structure rather than a sphere. We see from Figure 4.2.3 that Au nanoparticles take a polyhedral shape after a long enough annealing at high temperatures. The shape of the particles can be related to the low eutectic temperature (~373 °C) of Au-Si alloy [56].

In the second set of samples, we studied the Au films on ITO coated glass substrates. The annealing and other process parameters were the same as the previous sample set. The SEM images are given in Figure 4.2.3 and Figure 4.2.4.

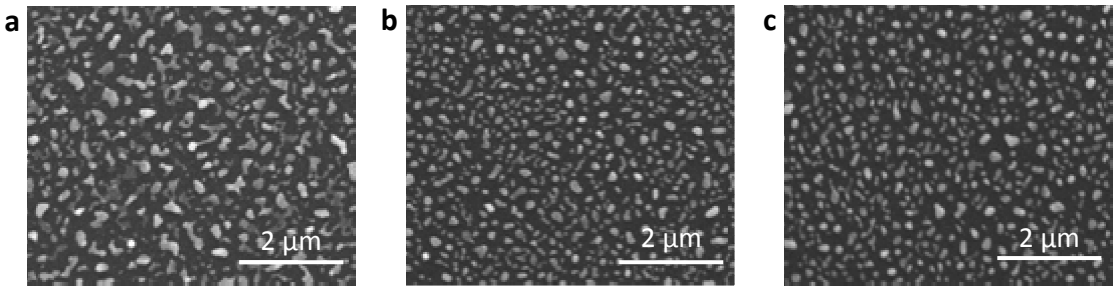

Figure 4.2.3 : SEM images of ITO/glass coated with 12 nm Au film which were annealed at 300 °C (a), 400 °C (b) and 500 °C (c) for an hour.

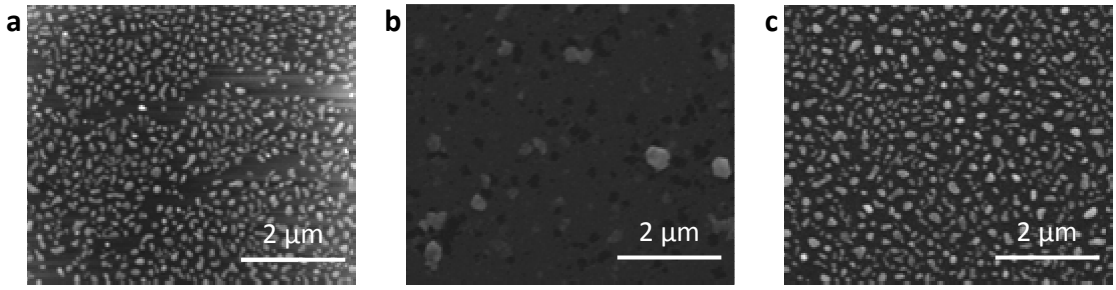

Figure 4.2.4 : SEM images of ITO/glass coated with 12 nm Au film which were annealed at 400 °C for 5 minutes (a), 15 minutes (b) and one hour (c).

The Au nanoparticles formed on ITO/glass substrate exhibit different character. We observe no indication for the crystallization. The irregularity in the form of the particles is quite obvious from the SEM images. We observe no specific shape formation at different annealing temperatures; the shapes of the particles are very irregular. In one particular sample annealed at 400 °C for 15 minutes, no regular nanoparticle formation is observed at all. This might be related to contamination of that particular sample's surface.

Following the first attempts with the Au nanoparticles, consecutive experiments were conducted with Ag nanoparticles. 12 nm Ag film was evaporated on (100) oriented Si and ITO coated glass in order to make a comparison between the effects of metals. Samples from this set were annealed at 200 °C, 300 °C, 400 °C and 500 °C, separately for one hour. The SEM images of Ag nanoparticles formed on Si wafer are shown in Figure 4.2.5 below.

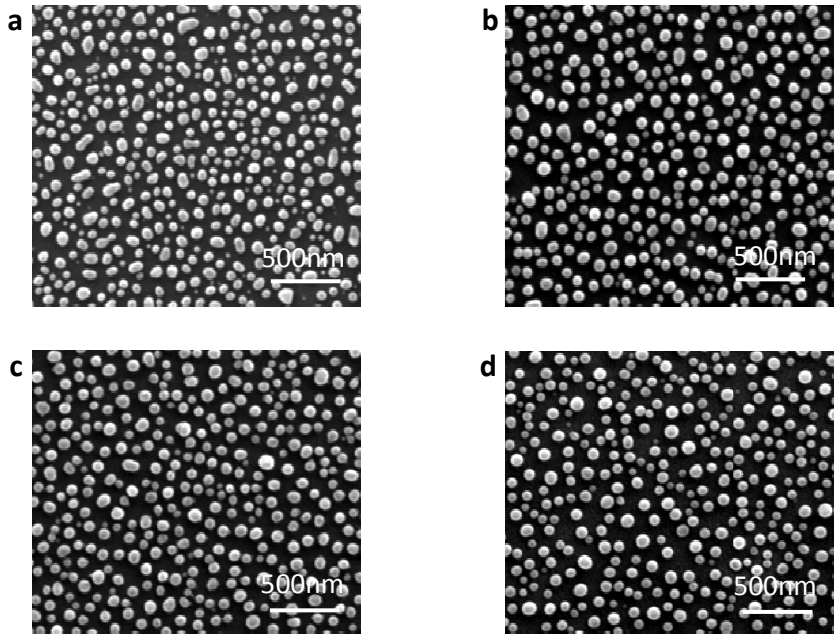

Figure 4.2.5 : SEM images of Si (100) wafers coated with 12 nm Ag film which were annealed at 200 °C (a), 300 °C (b), 400 °C (c) and 500 °C (d) for an hour

At the first sight, we see that the nanoparticles have much more regular shapes with less variation. The shape of the particles is mostly spherical which makes the optical analysis easier. The crystallization tendency is not observed with the Ag film. This is clearly due to the high eutectic temperature (845 °C) of Ag-Si system [57].

We conclude at this point that the eutectic temperature should be taken into the account when nanoparticles are formed on Si substrate. The images for the samples fabricated on the ITO coated glass substrate are shown in Figure 4.2.6 below.

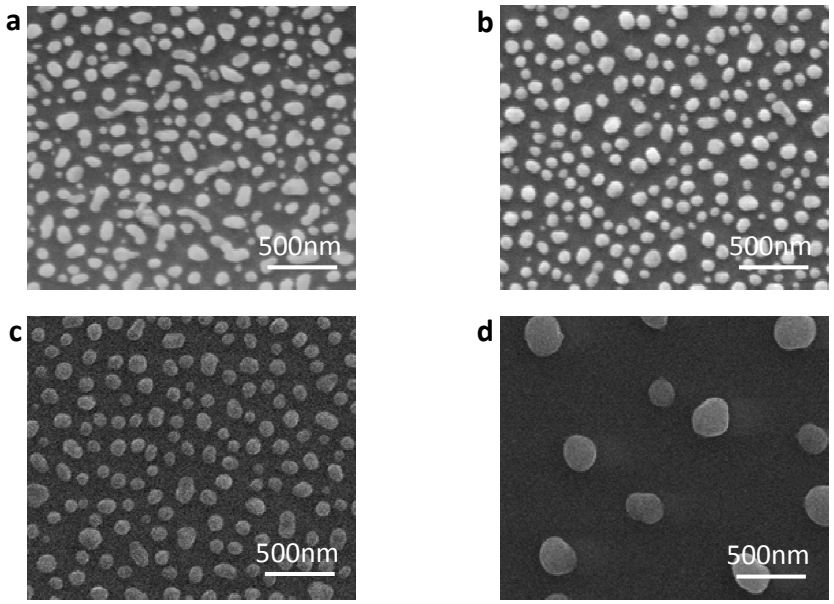

Figure 4.2.6 : SEM images of ITO/glass coated with 12 nm Ag film which were annealed at 200 °C (a), 300 °C (b), 400 °C (c) and 500 °C (d) for an hour

Again, we obtained more regular shapes and size distribution when compared to the Au nanoparticles. The distinct feature we observed with ITO/glass substrate is the variation with the temperature. The regularity of the nanoparticles improves substantially with the annealing temperature. In addition, the particle size increases with the annealing temperature.

We have presented results on Au and Ag nanoparticles formed on two different substrates. We can conclude that Ag nanoparticles are better defined in terms of shape, size and size variations compared to Au nanoparticles. Along with the optical advantages, the superior structural properties make Ag nanoparticles natural choice for the plasmonic applications.

4.2.1 Effect of Annealing Ambient

The size and the size distribution have detrimental effects on the plasmonic behavior of nanoparticles. For this reason, understanding and controlling the nanoparticle formation process is crucial. In this work, we have attempted to cover most of the process conditions to reach the optimum conditions for the nanoparticle formation. Instead of doing the annealing process in the furnace under N_2 atmosphere, metal evaporation and annealing processes were

combined by heating the sample in the e-beam evaporator chamber just after the evaporation. 12 nm Ag film was evaporated and then annealed under vacuum at 450 °C for 30 minutes. The SEM image of the surface is shown in Figure 4.2.7 below.

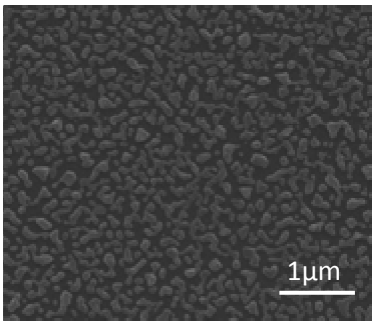

Figure 4.2.7 : SEM image of Si (100) which was coated with 12 nm Ag film and annealed under vacuum at 450 °C for 30 minutes

It is surprising enough to see that the film was dewetted mostly in the form of a network. Only a few individual nanoparticles could be formed. This structure is quite different than those annealed under N_2 flow. The questions arise "Has the dewetting process slowed down and resulted in an incomplete structure?" or "Is there another thermodynamic process taking place under vacuum?". In order to search for the answer to these questions and shed some more light on the nanoparticle formation, we have performed a series of experiments with Rapid Thermal Annealing (RTA) with which we have the possibility to process under vacuum condition.

The Ag coated samples were annealed under both vacuum and N_2 ambient. The comparison was made for two different temperatures; 300 °C and 500 °C as shown in Figure 4.2.8. The RTA annealing durations were chosen to be shorter because the RTA annealing is more effective than the furnace annealing, meaning that the sample is heated at a much faster rate than the furnace annealing.

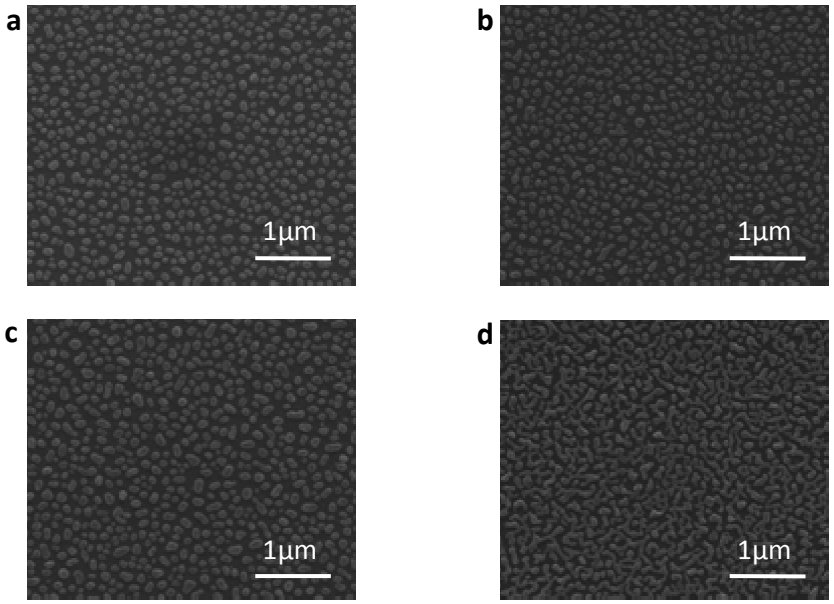

Figure 4.2.8 : SEM images of Si (100) wafers coated with Ag film which were annealed at 300 °C under N_2 flow for an hour (a), under vacuum for 30 minutes (b), at 500 °C N_2 flow for an hour (c) and under vacuum for 30 minutes (d)

Very interesting difference were observed between vacuum and N_2 annealings. At low temperatures, these two processes yielded fairly the same results in terms of particle size and distribution. The shape of the particles is slightly different for these two cases. However, when the annealing process was done at 500 °C lower particle population was obtained under N_2 annealing. More interestingly, the metal film annealed under vacuum did not generate discrete nanoparticles. Instead, a network of metal nanostructures has been obtained. This result is similar to the one obtained from the annealing process done in the e-beam chamber at 450 °C (see Figure 4.2.7). Here, we can conclude that the metal film has the tendency to form a network rather than discrete particles with the increase in annealing temperature. Most probably, particles, which had been formed at the earlier stages of the annealing, are reconnected to each other and then resulted in the observed network structure. As this happened only during the vacuum annealing, we believe that the thermodynamics of the metal particle formation is affected by the annealing environment. It is likely that the surface forces creating the surface structure is not strong enough to confine the metal atoms in the spherical shape under vacuum environment. As the environmental pressure on the surface should be very low under the vacuum condition, the surface forces can easily be overcome by the metal atoms to deform the spherical shape. This part of the study has revealed that the N_2 annealing is preferable over the vacuum annealing due to its superiority in shaping the resultant nanoparticles.

4.3 Image Analysis for Particle Size Determination

4.3.1 Analysis of Ag Nanoparticles on Si Substrates

In the previous section, the effect of temperature was considered in terms of homogeneity and the geometry of the nanoparticles on Si wafer and ITO substrate. In this section, more details on the image analysis of the samples prepared on different substrates are given to reveal different features of the nanoparticles and the effects of process parameters on them. For this purpose, SEM images from different set of samples were analyzed to obtain the mean size and the size distribution.

Formation of nanoparticles with the dewetting process was discussed in Chapter 3 from a theoretical point of view. As discussed there, nanoparticle formation was induced as a result of stress relaxation, surface diffusion, and lateral diffusion caused by the stress gradient. This is however only a part of the story. Once the nanoparticles are formed on the surface, another process takes place: Ostwald ripening. The behavior of nanoparticles under different annealing conditions could be understood with the help of Ostwald ripening concept which is widely used in various material processes. One of the requirements for the Ostwald ripening process is the mass conservation during the heat treatment, which is met during the metal nanoparticle fabrication from a predeposited thin film. In general the annealing of a structure on a foreign surface promotes the surface diffusion, during which small and big particles are formed.

To reach thermodynamically favorable conditions, small particles tend to shrink and join the larger ones. As a result, the average size of the system increases with prolonged annealing times. This is the typical process that takes place during the Ostwald ripening. In order to see whether this approach is applicable to the present case, we examined a couple of samples with the image analysis program called Gwyddion. Gwyddion was described in Chapter 3.

The results of the image analysis of the Ag nanoparticles obtained after 200 °C and 500 °C annealing are shown in Figure 4.3.1. The effect of the annealing temperature is clearly seen from the size statistics. The mean particle size, which is 67 nm for 200 °C and 66 nm for 500 °C, is almost the same for these two different annealing temperatures. This indicates that the particle size is determined not only by Ostwald ripening but other factors must also be

playing a role at 500 °C. On the other hand, the improvement in the homogeneity of the particle size with increasing annealing temperature is clearly visible both from the SEM images directly and from Full Width Half Maximum (FWHM) of the distributions of the particle size.

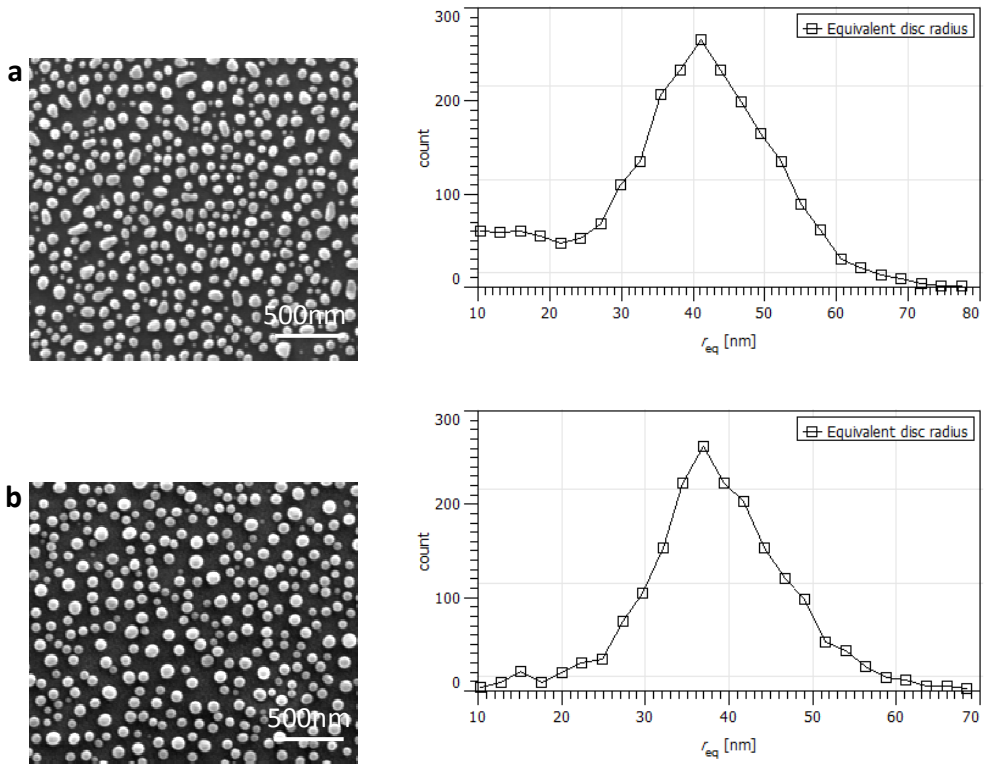

Figure 4.3.1 : (a) SEM image of Ag coated Si (100) which was annealed at 200 °C and its equivalent disc radius graph with FWHM of 19.3 nm (b) SEM image of Ag coated Si (100) which was annealed at 500 °C and its equivalent disc radius graph with FWHM of 16.3 nm

As the annealing temperature increases, the fraction of the small particles decreases. This has resulted in with a sharper distribution peak as we see from the graphs displayed in Figure 4.3.1. This can even be recognized from the SEM images by eyes.

4.3.2 Analysis of Ag Nanoparticles on SiO_2 and Si_3N_4 Substrate

We have studied the effect of substrate type on the nanoparticle formation with different underlying layers. For this purpose, Ag film was evaporated onto SiO_2 and Si_3N_4 layers formed on the Si substrate. This set of sample was exposed to same annealing procedure as

the other samples. The effect of the annealing temperature on nanoparticles formed on Si_3N_4 deposited Si wafer is shown in Figure 4.3.2 below.

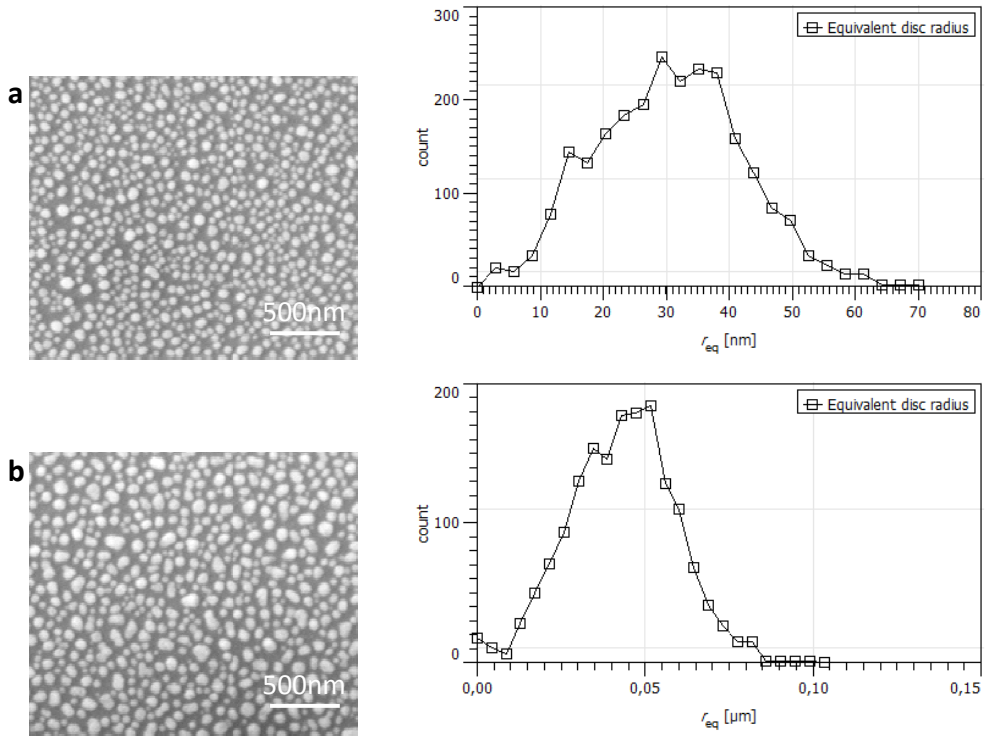

Figure 4.3.2 : SEM images and the equivalent disc radius graphs of Ag nanoparticles on Si_3N_4 deposited Si (100) wafers which were annealed at 200 °C (a) and 500 °C (b)

From the particle analysis, we see that the mean size increased from around 37.5 nm in the sample annealed at 200 °C to around 45 nm in the sample annealed at 500 °C. This is contrary to what we observed for the Si substrate where we observed almost no change in the particle size with annealing temperature. The reason for this difference is related to the interaction properties between metal nanoparticles and the underlying surface. It is clear that the thermal effect is more important for Si_3N_4 surface than Si surface.

The other dielectric layer used in our work was the SiO_2 layer. The SEM images of the nanoparticles formed on this substrate and their analysis are shown in Figure 4.3.3. The increase in the nanoparticle size was again observed with the annealing temperature. The mean diameter of the nanoparticles was increased from 53 nm to 107 nm. The size distribution graph approaches the Gaussian shape at high temperature as a result of improved uniformity. In addition, these SEM pictures clearly demonstrate the validity of the Ostwald ripening. We see the coexistence of small and large nanoparticles in the samples annealed at

200 °C. The number of small nanoparticles decrease with the annealing temperatures as expected from the Ostwald ripening process. As a result of this process, the total number of particles in the sample annealed at 200 °C is almost twice that of the sample annealed at 500 °C.

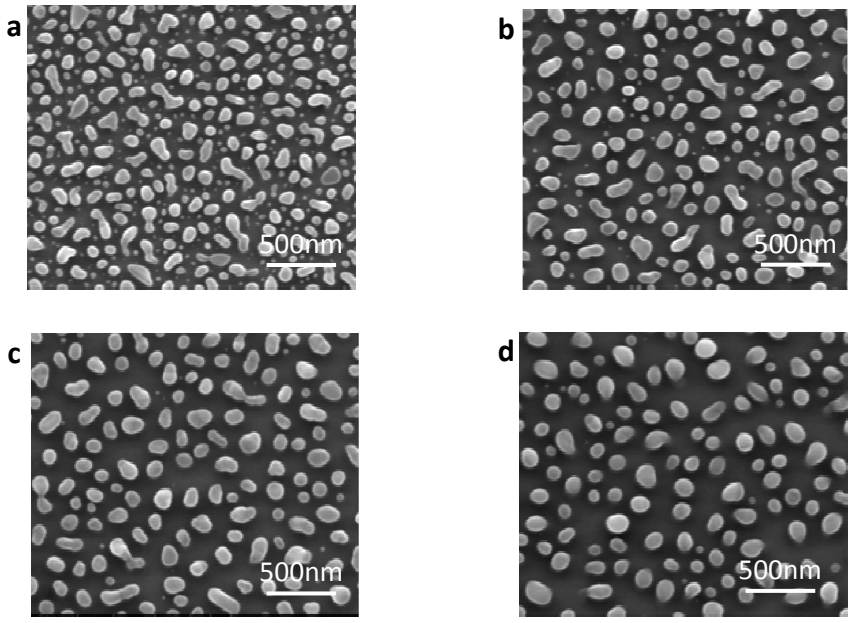

Figure 4.3.3 : SEM images of Si (100) wafers SiO_2 dielectric layer on it coated with 12 nm Ag film which were annealed at 200 °C (a), 300 °C (b), 400 °C (c) and 500 °C (d) for an hour

4.3.3 Ag nanoparticles on ITO Coated Glass

Another clear example for the Ostwald ripening is seen from the samples prepared on ITO coated glass substrates whose images were given in Figure 4.2.6

At 200 °C the particles are irregularly shaped. The size distribution is wide since FWHM of the equivalent disc radius graph is 33.8 nm. Moreover, when the temperature increased to 300 °C and 400 °C, the homogeneity in both shape and size distribution of the particles is almost established. However, it is very interesting to see that the particle size increased from 123 nm to 242 nm by increasing the annealing temperature from 400 °C to 500 °C.

In the Table 4.3.1 below, the evaluated mean diameters of Ag nanoparticles on each substrate are listed in order to make comparison between these sets.

Table 4.3.1 : Mean diameters of Ag nanoparticles on each substrate

Annealing temperature	Si	Si + Si_3N_4	Si + SiO_2	ITO/glass
200 °C	67 nm	75 nm	53 nm	105 nm
300 °C	74 nm	85 nm	81 nm	110 nm
400 °C	76 nm	88 nm	102 nm	123 nm
500 °C	66 nm	90 nm	107 nm	242 nm

The equivalent radius distributions of the metal particles both on Si and Si_3N_4 surface show a Gaussian profile with a narrow breadth which is also inferable directly from their SEM images. However, in the other two sets, SEM images of the samples annealed at 200 °C and 300 °C indicate the broad size variation without any dimensional analysis. On the other hand, increase in the annealing temperature highly affects these sets. The size of the particles dramatically increases with annealing temperature and small nanoparticles disappeared by being added to larger particles. As a consequence, the size distribution becomes homogeneous for high annealing temperatures. For a more quantitative understanding of the dewetting process, for this kind of studies, it could be advantageous to conduct atomic force microscope (AFM) based roughness measurements for exploring microscopic influence of annealing on various thin film morphologies.

4.4 Scattering Differences vs. Dewetting Temperature

The potential role of plasmonic particles in an opto-electronic device was discussed in the second chapter. Basically, there are two possible applications of plasmonic effects in solar cell device: near field effect and improved light trapping via scattering. In this work, we focused on the scattering effect from nanoparticles. The scattering from nanoparticles can be characterized by measuring the light reflected to all directions. Following the nanoparticle fabrication process, the scattering from the nanoparticles were measured using a reflection setup to measure at backward scattering configuration, which was introduced in the third chapter. In this section, the results from the scattering measurements obtained from different

sample sets are presented. Once the experimental setup is constructed, it is quite straightforward to obtain the plasmonic resonance peaks from the scattering measurements. However, these results should be complemented with the theoretical descriptions. The Mie theory was used in this study to obtain the scattering properties of spherical particles. Its physical background was discussed previously (see Chapter 2). We have used the "Mie light scattering by a single sphere" widget which is provided by the Nanophotonics group at Consejo Superior de Investigaciones Cientificas (CSIC) [58].

The scattering properties of Ag nanoparticles located on bare Si surface are shown in Figure 4.4.1 below. The difference in the scattering between bare Si and samples decorated with Ag nanoparticles verifies that the plasmonic particles manifest themselves in clear LSP peaks. The mean particle size obtained using Gwyddion and corresponding resonance peak positions are displayed in Table 4.4.1.

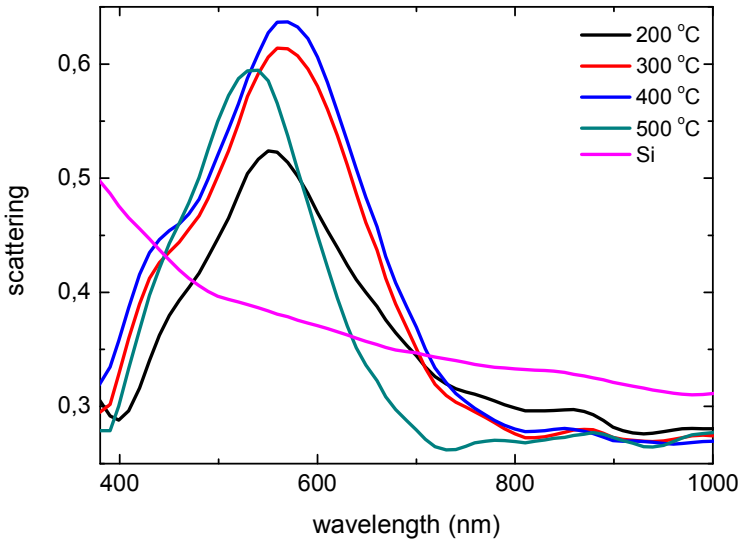

Figure 4.4.1 : Scattering of Ag nanoparticles annealed at different temperatures on Si surface

Table 4.4.1 : Mean diameter and peak positions of nanoparticles on Si surface for given annealing temperatures

Annealing Temperature	Mean Diameter	Peak Position
200 °C	67 nm	556 nm
300 °C	74 nm	569 nm
400 °C	76 nm	570 nm
500 °C	66 nm	535 nm

The particle size increases until 400 °C. An interesting observation is that the annealing at 500 °C has led to a reduction in particle size. We believe that this can be regarded to result from a reduction in the boiling point of Ag in the quasi 2D thin film form with respect to the bulk [59]. This view can be supported by the very observation of the dewetting process taking place at a low temperature range of 200-500 °C with respect to the melting point of ~960 °C for bulk Ag **[60]**.

The resonance peak position perfectly follows the size variation. The resonance peak redshifted with increasing size, and blueshifted with decreasing size. The size effect can be described as follows: When the particle size gets larger, the electrons at the conduction band tend to move out of phase with the incident electric field. For this reason, the depolarization field decreases and as a consequence the restoring force is reduced. This results in a redshift in the resonance peak position [61].

The scattering from a particle depends on the dielectric properties of the particle and the surrounding medium. In the present case, particles are not surrounded by a uniform medium. Some part of the particle touches the underlying substrate and some part of it is in the air. In order to make meaningful estimation from the theoretical considerations, the overall dielectric structure generating the observed scattering spectra should be defined. To do this we defined an effective dielectric constant which is related to the contact areas of the particle to the surrounding media. Except for the sample set made on Si wafer with Ag nanoparticles, the upper and lower media were considered to contribute equally to the effective dielectric constant of the particles. For this reason, the geometric average of the dielectric functions of each medium was taken as the dielectric function of the effective medium. The layers on the

substrate were obtained by deposition; because of that inhomogeneity for these layers is unavoidable. Since there is no extra layer for the sample set prepared on the bare Si wafer, the portion of the contact area with air was taken as 77% and 23% with Si. The image analysis was conducted for each sample over one SEM image, for this reason the diameters were not so accurate. Only one of the samples from each set was chosen for a representative analysis between theory and experiments.

The comparison between the peak positions of the sample annealed at 400 °C with a mean diameter 76 nm in a medium with a relative dielectric constant of 3.5 is shown in Figure 4.4.2 below. The calculations are done by using the Mie theory for spherical particles with given material, size and surrounding medium specifications.

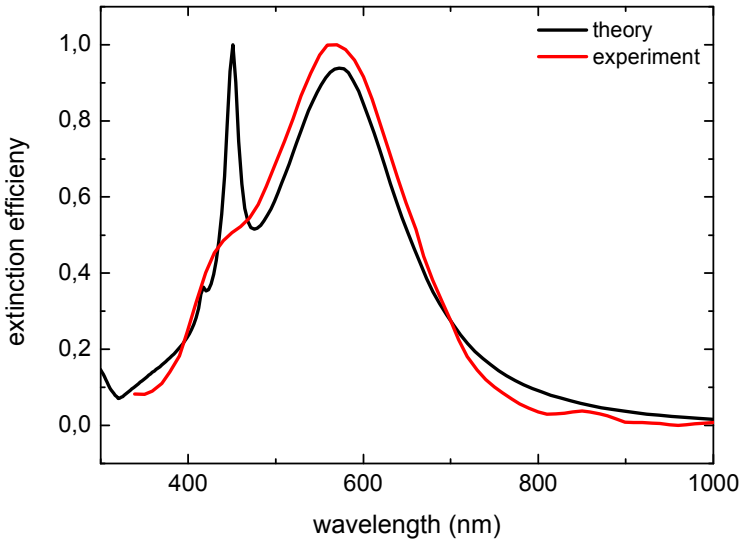

Figure 4.4.2 : Resonance peak positions obtained both from theory and experiment for Ag nanaoparticles on Si surface with a mean diameter of 76 nm

The main peak positions are 570 nm and 572.5 nm from experiment and theory, respectively. The peak positions of the other samples from this set shift to higher or lower wavelength depending on the variations in the particle size. The main peak seen in both experimental and theoretical curves is due to the plasmonic resonance of dipole oscillations. The sharp theoretical peak seen at around 450 nm is the quadrupole term which is sensitive to the interparticle interaction. In the experimental data, the quadrupole term is seen only as a kink on the main dipole scattering peak. It is smoothed due to the interaction between nanoparticles and the particle size variation.

The scattering from the sample set prepared on Si_3N_4 layer formed on Si wafer are shown in Figure 4.4.3. As expected in solar cell applications, the Si_3N_4 layer minimized the scattering from the surface.

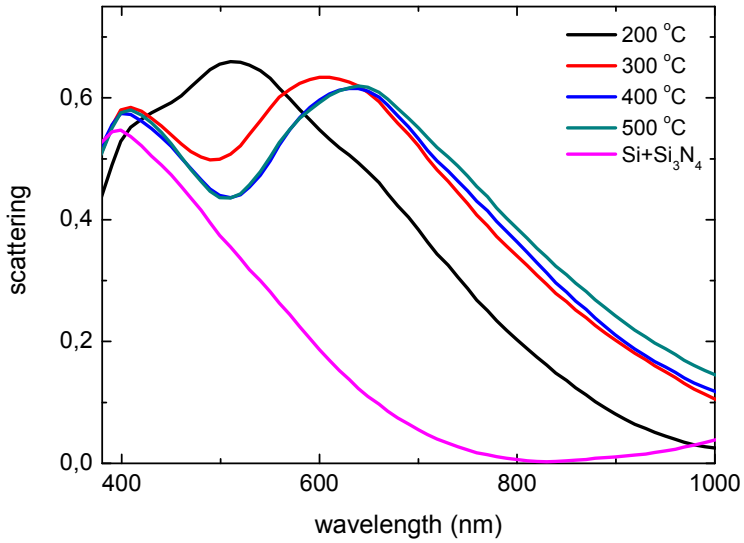

Figure 4.4.3 : Scattering of Ag nanoparticles annealed at different temperatures on Si_3N_4 surface

In Table 4.4.2 below, the mean diameters and resonance peak positions are listed for each sample in this set.

Table 4.4.2 : Mean diameters and resonance peak positions of nanoparticles on Si_3N_4 surface for given annealing temperatures

Annealing Temperature	Mean Diameter	Peak Position
200 °C	75 nm	517 nm
300 °C	85 nm	611 nm
400 °C	88 nm	636 nm
500 °C	90 nm	642 nm

In this case, the particle size increases monotonically with annealing temperature. The scattering spectra show an excellent correlation with the size variation. The plasmonic resonance peak position shifts to higher wavelengths with increasing temperature. The plasmonic peaks are located at a higher wavelength compared to the Si substrate because of the larger particle size and dielectric function of the effective medium as expected from Mie theory. Moreover, quadrupole peaks are noticeable for the samples annealed at temperatures higher than 200 °C. As mentioned earlier, higher order modes become nonnegligible, for the particles with larger sizes.

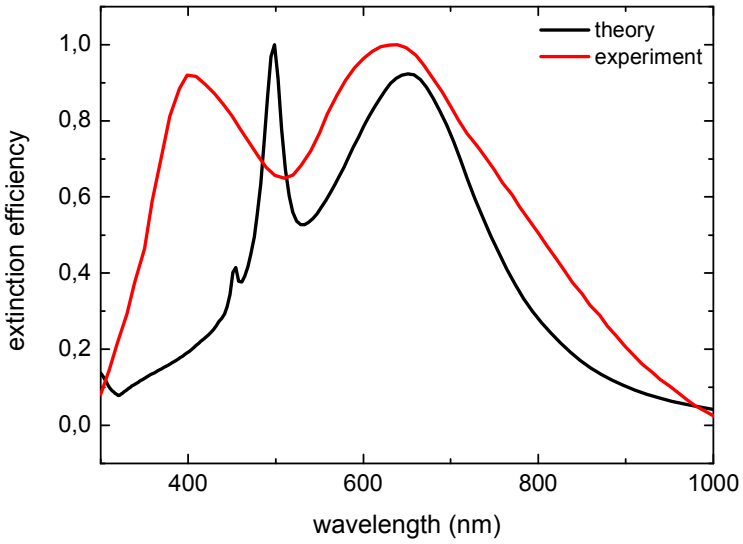

Figure 4.4.4 : Resonance peak positions obtained both from theory and experiment for Ag nanoparticles on Si_3N_4 surface with a mean diameter of 88 nm

The comparison with the theory was done for the sample annealed at 400 °C in Figure 4.4.4 above. The theory was applied by using the concept of the effective dielectric medium as above. The dielectric constant was taken to be 4.25 in this case. As seen from Figure 4.4.4, the dipole peaks of both theory and experiment are almost at the same wavelength; however the observed higher order modes do not match with the theoretically calculated values.

In the third set of samples, Ag nanoparticles are on a SiO_2 layer thermally grown on Si substrate. The scattering spectra of the SiO_2 surface and clear plasmonic resonances of the annealed samples at various temperatures are shown in Figure 4.4.5.

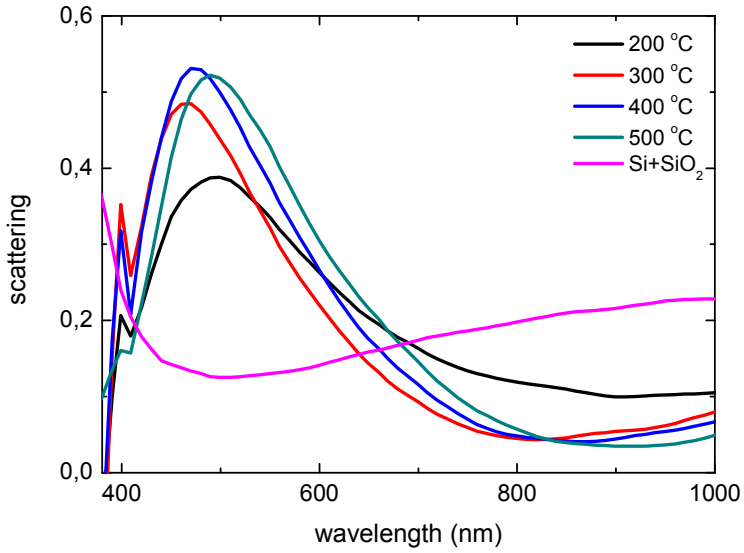

Figure 4.4.5 : Scattering of Ag nanoparticles annealed at different temperatures on SiO_2 surface

The sample annealed at 200 °C exhibits an anomalous behavior in this set. Although the mean diameter of that sample evaluated from dimensional analysis is the smallest in this sample, its peak is the broadest and relatively redshifted with respect to the samples having larger mean sizes. The results of dimensional analysis and the peak positions are shown in Table 4.4.3.

Table 4.4.3 : Mean diameters and resonance peak positions of nanoparticles on SiO_2 surface for given annealing temperatures

Annealing Temperature	Mean Diameter	Peak Position
200 °C	53 nm	497 nm
300 °C	81 nm	466 nm
400 °C	102 nm	475 nm
500 °C	107 nm	493 nm

The anomalous result obtained from the sample 200 °C needs to be explained. From the image analysis, we find that the particle population for the sample annealed at 200 °C is

higher than the others. For example, the number of particles obtained under 400°C is one third of the ones obtained under 200 °C. The high population causes more interaction between particles. Since the increased interaction between nanoparticles approaches physical contact between nanoparticles, the particle size can be assumed to be increased effectively. In addition, the size distribution is expected to be broader in the samples annealed at low temperatures. In the equivalent disc radius graphs shown in Figure 4.4.6 below, we see indeed that the sample annealed at 200 °C has a much wider size distribution than the sample annealed at 400 °C. It is even hard to define a statistically meaningful mean size for this sample.

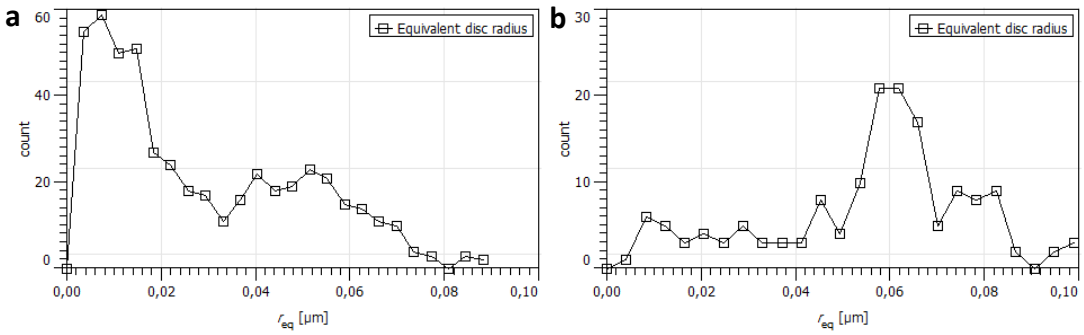

Figure 4.4.6 : Equivalent disc radius graphs of nanoparticles on SiO_2 surface which are obtained at 200 °C (a) and 400 °C (b)

Nevertheless, a mean size is calculated mathematically and found to be low. However, the presence of large particles seen from the Figure 4.4.6 above and the interaction between nanoparticles leads to a condition where effective mean diameter is larger than the apparent sizes especially for the sample annealed at 200 °C. For this set of samples, the one annealed at 500 °C was chosen for the comparison with the theory, since we obtained the most uniform distribution thus, most accurate dimensional analysis from this sample. The dielectric constant of the effective medium was taken to be 3.03 under the approximation explained above.

As it is seen from the graph given in Figure 4.4.7, higher order term cannot be detected from the scattering measurements.

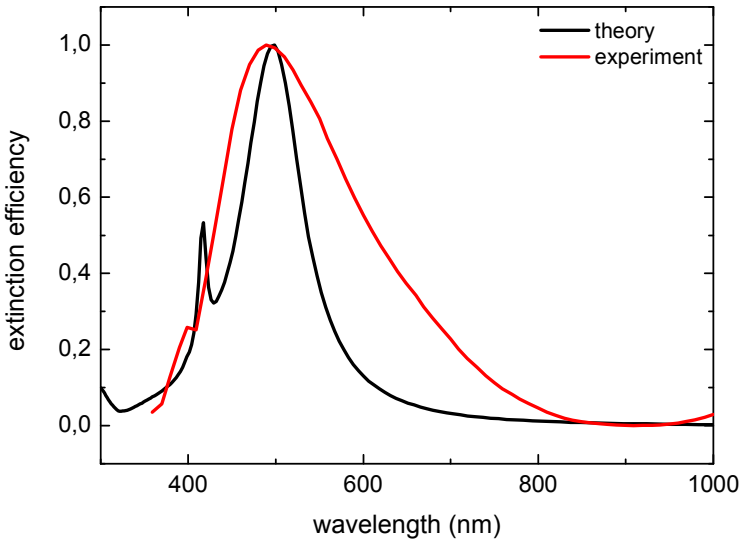

Figure 4.4.7 : Resonance peak positions obtained both from theory and experiment for Ag nanoparticles on SiO_2 surface with a mean diameter of 107 nm

Finally, we have characterized nanoparticles on prepared ITO coated glass. The scattering spectra of this sample set are shown in Figure 4.4.8.

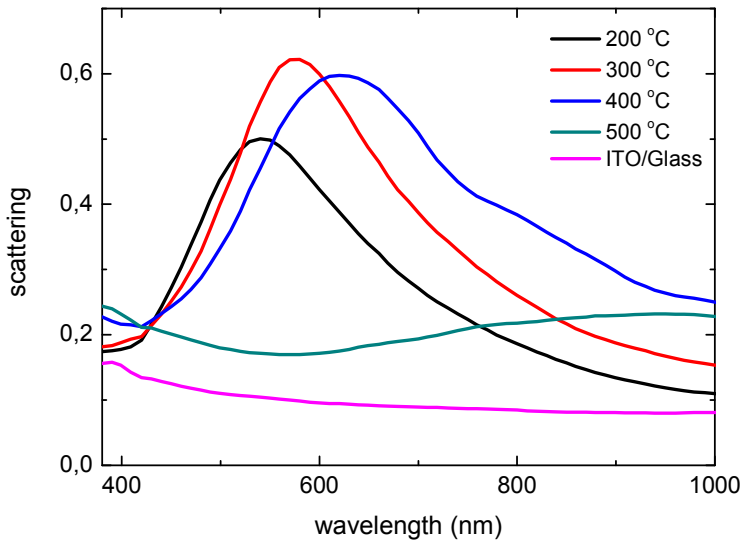

Figure 4.4.8 : Scattering of Ag nanoparticles annealed at different temperatures on ITO surface

The striking feature of the ITO samples is the sudden increase in the particle size after 500 °C annealing. The effect of this variation is clearly seen in the scattering spectra. The position of the resonance peak redshifts monotonically with increasing particle size for annealing temperatures of 200 °C, 300 °C and 400 °C as observed in other studied samples.

Table 4.4.4 : Mean diameters and resonance peak positions of nanoparticles on ITO surface for given annealing temperatures

Annealing Temperature	Mean Diameter	Peak Position
200 °C	105 nm	540 nm
300 °C	110 nm	580 nm
400 °C	123 nm	630 nm
500 °C	242 nm	~970 nm

In agreement with the large increase in the particle size, the peak position for the sample annealed at 500 °C shifted towards the infrared region with a big jump. The signal has also broadened, so that it is hardly possible to identify an accurate local maximum. Due to this effect and difficulties of measurement outside the visible region, an approximate peak value was recorded for this sample in Table 4.4.4. The theoretical calculation for the sample annealed at 400°C was carried out by taking the effective dielectric constant for this sample. The result is shown and compared with the experimental data in Figure 4.4.9.

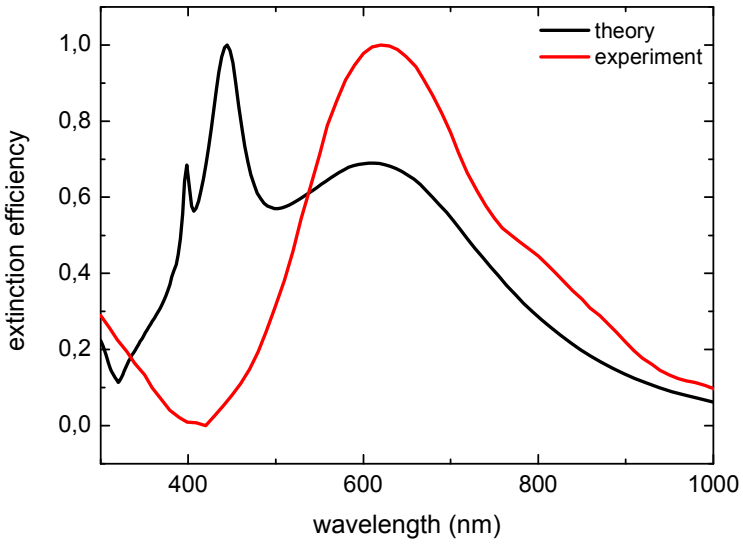

Figure 4.4.9 : Resonance peak positions obtained both from theory and experiment for Ag nanoparticles on ITO surface with a mean diameter of 123 nm

As in the previous sample set, the higher order modes could not be observed in the scattering measurements. However, the experimental and theoretical dipole peaks are very well agreed with a small shift with respect to each other. Quadrupole, octupole and the other higher order modes are much more dependent on the shape of the particles and the particle-particle interaction than dipole mode. The interparticle distance control is weak in dewetting technique when compared with EBL. For these reasons, higher order modes are hardly detectable in our scattering measurements.

As seen in the equivalent disc radius graphs, the size distributions are not sharp. Moreover, we consider perfect spherical geometry in our simulations. Therefore, exact particle geometry being different than perfect sphere can account for the absence of the higher order modes in the experiment, which are present in the theoretical curves. In addition, the particles in our experiment are in inhomogeneous media. This inhomogeneity expectedly disturbs the symmetry in scattering. When we consider all these differences between the simulations done for idealized cases and the far-from-perfect real systems, the relatively good match between the two curves is a notable success within a 20 nm resonance peak position coincidence.

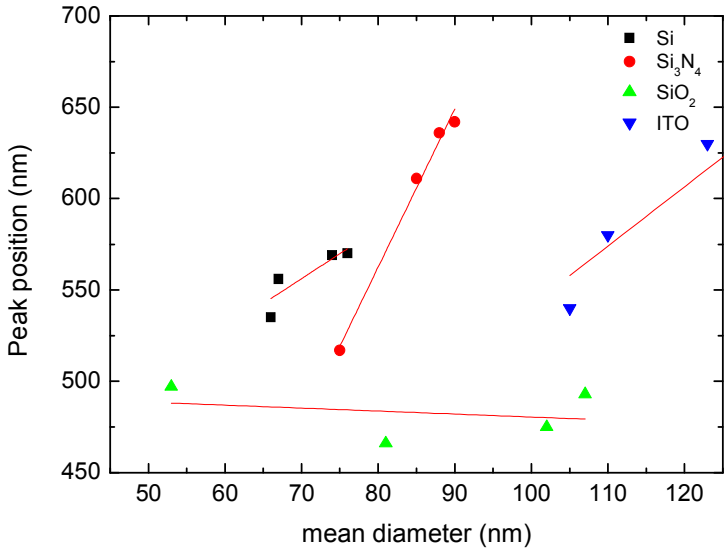

Figure 4.4.10 : Graph of resonance peak position vs. mean diameters of nanoparticles on all types of surfaces used

The variation of resonance peak position with the mean particle size is summarized in Figure 4.4.10 for all sample types. We see that the peak position shifts to red with increasing particle size for all sample types except for SiO_2 samples annealed at low temperatures. The anomaly seen in SiO_2 needs special attention and analysis. As discussed in the previous section, nanoparticles formed on SiO_2 phase have a peculiar distribution. It contains group of very small and very big nanoparticles. The dimensional analysis exhibits two peaks at around 15 nm and 50 nm. Although the mean particle size is found to be 53 nm mathematically, larger particles dominate the scattering process due to the fact that the scattering of smaller particles is weak and only absorption is effective in the total light extinction of small particles. For this reason, the peak position does not correlate with the nanoparticle size for these samples. As indicated in Figure 4.4.5, the actual particle size that is effective in the scattering process should be more than the apparent size. If we entirely neglect the small particles, the equivalent disc radius comes around 50 nm and this brings the scattering data to a very meaningful point. In the spectrum as shown in Figure 4.4.10, we should also address the dependence of particle size-resonance peak position relation on the underlying layer. We have clearly demonstrated in this work that the resonance peak position redshifts with increasing particle size for a given sample type. However, the peak position varies with the substrate type for a given particle size. This dependence should be related to

the dielectric properties of the underlying layer. In Figure 4.4.11 below, the resonance peak positions obtained from experiments for particles on Si, Si_3N_4 and SiO_2 surfaces, which have similar mean diameters, and a line which represents the variation in peak position with dielectric function of the surrounding medium for a spherical particle. The radius of the spherical particle is taken as 38.5 nm, which is the average of the particle sizes on the surfaces dealt in this graph.

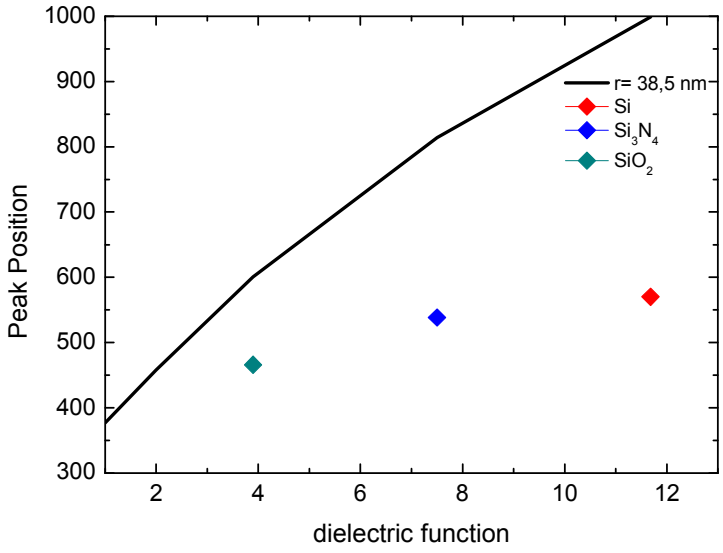

Figure 4.4.11 : Graph of resonance peak position vs. dielectric function of surrounding medium of a particle with 38.5 nm radius

The resonance peak position redshifts with increasing the dielectric function of the surrounding medium as expected from the black curve. The reason that the color points do not fall right on the black curve is because the particles in the experiment are not fully immersed in the substrate. However the effective index of refraction surrounding the particles scale up correlated with the index of refraction of the substrate which is substantially different than that of air.

4.5 Fabrication of Ag Nanoparticles on the Textured Surface of Crystalline Si Solar Cells

One of the major applications of plasmonic structures is to use them on solar cells for efficiency improvement. Although our aim was not to demonstrate the device application in this thesis work, we studied formation of Ag nanoparticles on textured solar Si wafers with or without nitride coating. This material system is exactly the same as the one used in industrial solar cell applications. The results are presented and briefly discussed in this section.

Crystal Si based solar cells have textured surfaces to reduce the reflection from the surface. Therefore, the effect of textured morphology on the formation of metal nanoparticles should be examined if these systems will be utilized in applications. Surface of the Si wafer was textured by anisotropic etching in aqueous solution containing potassium hydroxide (KOH) with a concentration of 6.3%, DI water and IPA at 85 °C for 45 minutes [62]. The SEM image of a typical surface is shown in Figure 4.5.1 below.

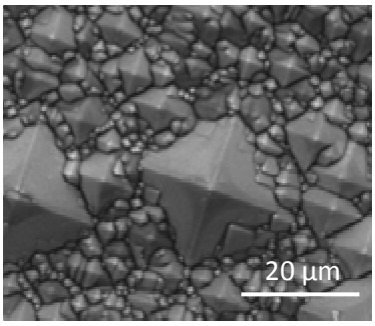

Figure 4.5.1 : SEM image of a typical textured Si surface

The prepared surface textured Si wafers were exposed to same process conditions after the metal film evaporation to induce metal nanoparticle formation. The samples processed identically as all other samples are shown in Figure 4.5.2.

Figure 4.5.2 : The samples are lined up as 12 nm Ag film coated on surface textured Si, annealed at 200 °C, 300 °C, 400 °C and 500 °C, respectively.

The sample annealed at 500 °C has a distinctly different color than the rest of the set. This fact is clearly evident in the scattering measurements (see Figure 4.5.3). The resonance peak position of the sample annealed at 500 °C is apparently blue shifted, while the resonance peak positions of the other samples are close to each other.

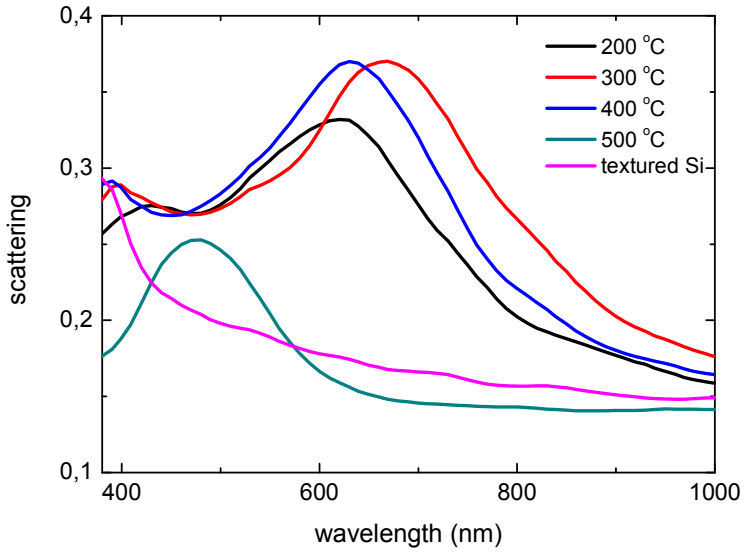

Figure 4.5.3 : Scattering of Ag nanoparticles annealed at different temperatures on textured Si surface

The SEM images of the samples with Ag nanoparticles are shown in Figure 4.5.4. The sample annealed at 200 °C is shown with a lower magnification in order to see the pyramids formed on the surface. Ag nanoparticles are seen in the images with the higher magnification. We see that Ag nanoparticles are uniformly formed everywhere on the

pyramid structure. We notice no dependence on the surface orientation. Both the top of the pyramids and valleys between them are fully covered by the Ag particles. Because of the visual deformation due to high slopes on pyramid facets, it is hard to perform a reliable dimensional analysis. However, we can estimate their sizes to be around 90±2 nm. These results are showing that the formation of nanoparticles on textured surfaces does not have any complication and this process can be applied to solar cells.

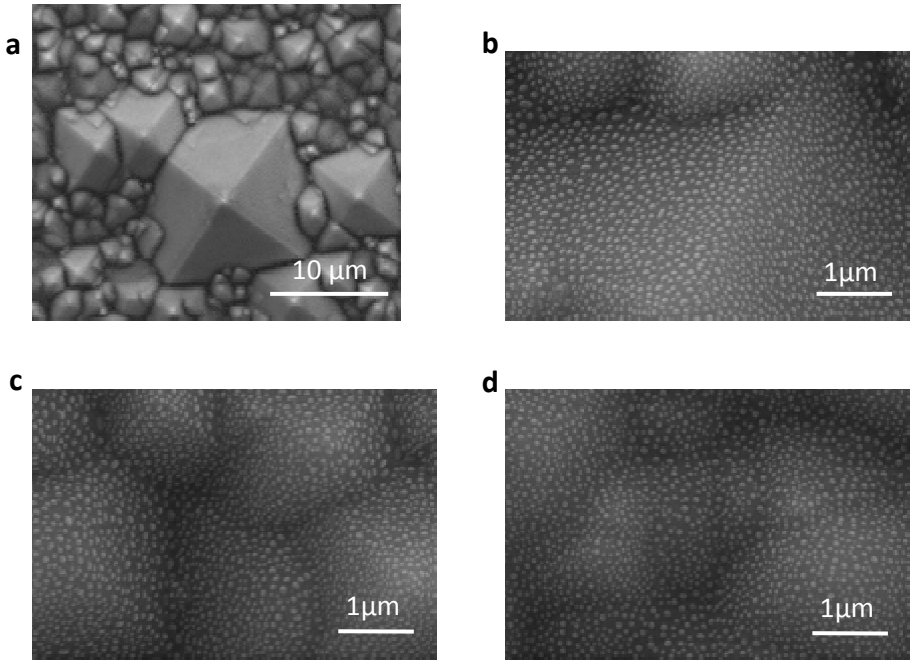

Figure 4.5.4 : SEM images of textured Si (100) wafers with 12 nm Ag film which were annealed at 200 °C (a), 300 °C (b), 400 °C (c) and 500 °C (d) for an hour

The textured surfaces of crystalline Si solar cells are usually covered with Si_3N_4 as an anti reflection layer. In order to test the applicability of dewetting on such realistic surfaces, we performed experiments. After the surface texturing, Si_3N_4 was deposited on the wafer with thickness of 75 nm which provides the best antireflection property for the solar spectrum. The rest of the processes are the same as the previous sample set. The photograph of the processed samples is shown in Figure 4.5.5. We see that the color of the sample surface is changing with the annealing temperature. This is indicating the variation in the nanoparticle size.

Figure 4.5.5 : The samples are lined up as 12 nm Ag film coated on surface textured Si with Si_3N_4 layer on it, annealed at 200 °C, 300 °C, 400 °C and 500 °C, respectively.

Similar to the case of Figure 4.5.2, in this set of samples, the one annealed at 200 °C seems apparently different than the others regarding the colors. The color transition is from blue to yellow with increasing annealing temperature as can be seen in Figure 4.5.5. The results of scattering measurements for this set of samples are shown in Figure 4.5.6 below.

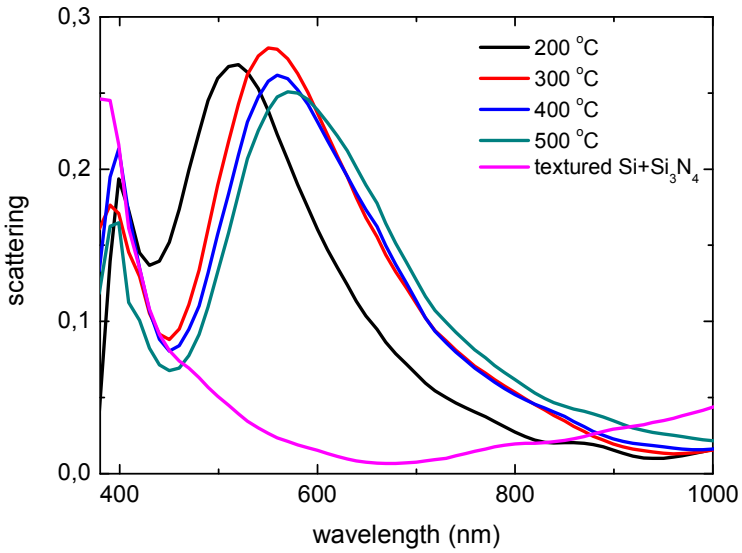

Figure 4.5.6 : Scattering of Ag nanoparticles annealed at different temperatures on textured Si with Si_3N_4 layer on it

The shifting of resonance peak position in scattering measurements verifies our expectations from the appearance of the samples after annealing. The peaks are red shifted with the annealing temperature. Moreover, the widest distance between the peaks is observed between the peaks of samples annealed at 200 °C and 300 °C. This result is also consistent

with their colors. The SEM images of the annealed samples are shown in Figure 4.5.7. Again, the image of the sample annealed at 200 °C is shown with a lower magnification to view the pyramid.

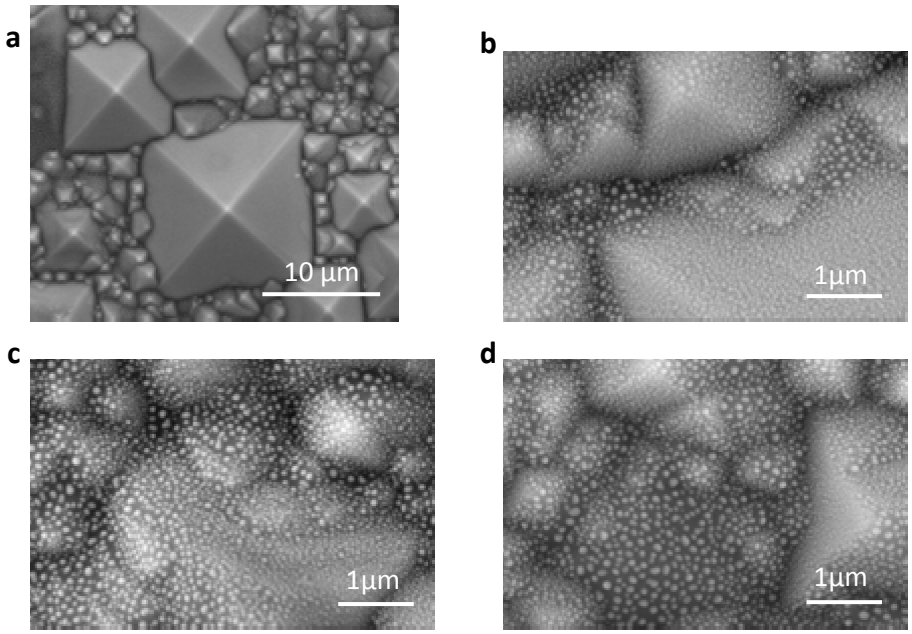

Figure 4.5.7 : SEM images of Si_3N_4 layer on textured Si wafers with 12 nm Ag film which were annealed at 200 °C (a), 300 °C (b), 400 °C (c) and 500 °C (d) for an hour

As discussed above, a quantitative dimensional analysis is hard. The size of the nanoparticles on Si_3N_4 increases from 56 nm to 73 nm, with the increasing annealing temperature from 200 °C to 500 °C. As in the textured Si case, the nanoparticles can be formed successfully. However, the size and shape of the particles are slightly different for two sets. The first obvious difference is in the mean particle size and the second one is in the surface coverage. The particle formation and coverage on a single flat inclined side surface of the pyramid for both textured Si and Si_3N_4 substrates are displayed in Figure 4.5.8. Contrary to the sets of flat surfaces, the mean diameters of the metal nanoparticles are larger on textured Si surface. The differences in the scattering data of the flat and textured surfaces cannot be explained by Mie theory.

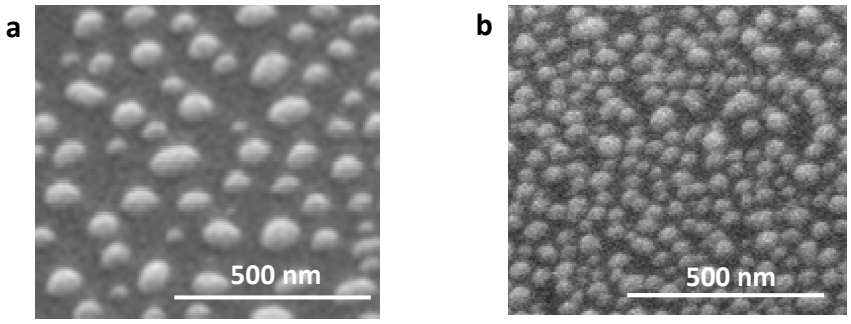

Figure 4.5.8: SEM images of one side of the pyramids on textured Si(a) and textured Si surface with a Si_3N_4 layer(b)

CHAPTER 5

CONCLUSIONS

In this M.Sc. thesis work, the fabrication of metal nanoparticles, their structural and optical properties have been investigated for the possible plasmonic applications. The metal nanoparticles were fabricated by EBL and dewetting techniques. Although EBL provides regularly shaped particles with controllable distances between them, it is a time consuming process which is not suitable for large area applications. Nevertheless, EBL is very useful for the proof of principle studies for academic purposes. On the other hand, the dewetting technique represents a method of fabrication for metal nanoparticles which can be directly applied to large areas. For this reason, the dewetting technique has been chosen as the major method of sample preparation in this study.

The most commonly used metals are Au and Ag in plasmonic applications. At the beginning of this study, both metals were used and compared from the fabrication point of view. We found that the Au film tends to crystallize under the process conditions we used. We attributed this crystallization effect to low eutectic temperature of the Au-Si alloy. We conclude that Au-Si alloy is formed in the crystalline form when the temperature of the annealing exceeds the eutectic temperature. Apart from fabrication drawbacks, Au is known to absorb incident light more than Ag. With these observations and considerations about Au, we decided to continue our study with Ag after this point.

For the fabrication of Ag nanoparticles 12 nm Ag thin film was thermally evaporated on various solar cell relevant surfaces and annealed at 200 °C, 300 °C, 400 °C and 500 °C for one hour in this study. In order to observe the effect of the surrounding medium on both the structural and the optical properties of metal nanoparticles, different dielectric layers such as SiO_2 and Si_3N_4 were deposited (or grown) on Si surface. The SiO_2 layer was grown by dry

oxidation and Si_3N_4 was deposited by PECVD. In addition, ITO on glass substrates were also utilized.

We looked at the particle formations and studied possible effects of different substrates. After the dimensional analysis, we observed that mean diameters for each set of sample at the same annealing conditions were quite different. Moreover, the geometry of the particles was also affected by the type of the substrate. When we scanned the annealing temperature, we found that the size of the metal nanoparticles on SiO_2 and ITO dramatically increased with annealing temperature. The Ostwald ripening was most clearly observed for this set of samples. It is likely that the large particle sizes we obtained for these substrate is related to effectiveness of the Ostwald ripening process.

The particle formation was also done on textured surfaces in order to observe the applicability of this fabrication method to a standard Si based solar cell. The surface of Si was textured by KOH solution. In some cases, the surface was covered with a Si_3N_4 layer, which is used as anti-reflective coating in solar cell technology. We have shown that nanoparticles were formed also on the textured surfaces similar to flat surfaces. However, the difference in mean diameters of particles could not be detected by dimensional analysis due to the difficulties in imaging of textured surfaces.

For the optical characterization, plasmonic resonance peaks were monitored for each sample set. Except for the set of samples with SiO_2 layer, the peak position was consistent with size of the nanoparticles. The peak position of the plasmonic resonance shifted to higher wavelengths with increasing nanoparticle size. The SiO_2 set needed special attention. In this sample set, the samples annealed at lower temperatures showed smaller particle mean size, while their plasmon peak is located at a higher value. When we analyzed the distribution in this sample we observed that there is a high population of very small nanoparticles together with the large nanoparticles. The mathematical analyses of this system yielded a mean value, which is largely determined by the small nanoparticles. However, the scattering yield of large nanoparticles is higher than the small nanoparticles. This is not only due to the geometrical factor, but also due to the higher absorption by the small nanoparticles. For these reasons, SiO_2 samples showed an anomaly especially in the samples annealed at relatively low temperatures.

We compared the experimental results with the theory. Actually, it is quite hard to match these results due to the uncertainties in system we have used in this study. The deposited

dielectric layers were not perfectly homogenous, and this directly influenced the formation of particles. The shape of all particles was not spherical and not well defined. Moreover, the dielectric functions of the media below and above the particle were contrasting. Under these circumstances, theoretical simulation of our system and a quantitative comparison with the experimental results are not an easy task. Mie theory was applied with some approximations for size, geometry and surrounding medium for our samples. The effect of dielectric layer was examined for Si, SiO_2 and Si_3N_4 surfaces by comparing the plasmonic peak position of the samples having similar mean diameters. We have found that the resonance peak positions were red shifted with effective dielectric function. This observation confirms the expected behavior of the plasmonic oscillations in metal nanoparticles.

In a nutshell, we have experimentally demonstrated the feasibility of the dewetting procedure for decoration of various kinds of substrate materials, from conductive (ITO) to insulating (SiO_2, Si_3N_4) as well as semi-conducting (Si), with metal nanoparticles for areas in the range of hundreds of square centimeter. These substrate materials were also chosen such that they constitute the most relevant materials that are used in the silicon based solar cell fabrication technology; some serving as top, and some serving as the intermediate layers in solar cell architecture. This way a preliminary understanding of the feasibility of the use of dewetting technique for incorporation of polasmonic metal nanoparticles at different positions in the solar cell architecture is achieved. This work was complemented by an experimental analysis of structural and optical properties of metal nanoparticle decorated substrates and also by theoretical modeling using the corresponding parameters as deduced from the experiments. Further examinations in the direction of targeted and controlled application of plasmonic oscillations to devices like solar cells can be conducted in the light of the results achieved in this thesis work.

REFERENCES

[1] Faraday M., Phil. Trans. R. Soc. Lond. **147**, 145 (1857).

[2] Garnett J. C. M., Phil. Trans. R. Soc. Lond. **203**, 385 (1904).

[3] Mie G., Ann. Phys. **25**, 377 (1908).

[4] Otto A., Z. Phys. **216**, 398 (1968).

[5] Kretschmann E., Z. Phys. A **241**, 313 (1971).

[6] Bouhelier A., Novotny L., Surface Plasmon Nanophotonics **131**, 139 (2007).

[7]Stuart H. R., Hall D. G., Appl. Phys. Lett. **73**, 3815 (1998).

[8] Schaadt D. M., Feng B. and Yu E. T., Appl. Phys. Lett. **86**, 063106 (2005).

[9] Lim S. H., Mar W., Matheu P., Derkacks and Yu E. T., J. Appl. Phys. **101**, 104309 (2007).

[10] Kim S.-S., Na S.-I., Jo J., Kim D.-Y. And Nah Y.-C., Appl. Phys. Lett. **93**, 073307 (2008).

[11] Yoon W.-J., Jung K.-Y., Liu J., Duraisamy T., Revur R., Teixeira F. L., Sengupta S. and Berger P. R., Sol. Ener. Mat. Sol. Cells **94**, 128 (2010).

[12] Fahr S., Rockstuhl C. and Lederer F., Phot. Nano. Fund. Appl. **8**, 291 (2010).

[13] Haegglund C., Zaech M. and Kasemo B., Appl. Phys. Lett. **92**, 013113 (2008).

[14] Ferry V. E., Verschuuren M. A., Li H. B. T., Schropp E. I., Atwater H. A. and Polman A., Appl. Phys. Lett. **95**, 183503 (2009).

[15] Derkacs D., Lim S. H., Matheu P., Mar W. and Yu E. T., Appl. Phys. Lett. **89**, 093103 (2006).

[16] Kim J., Abou-Kandil A., Fogel K., Hovel H. and Sadana D. K., ACS Nano **4**, 7331 (2010).

[17] Pillai S., Catchpole K., Trupke T., Zhang G., Zhao J. and Green M. A., Appl. Phys. Lett. **88**, 161102 (2006).

[18] Chandramohan S., Ryu B. D., Uthirakumar P., Kang J. H., Kim H. K. and Kim H. G., Solid-State Elctronics **57**, 90 (2011).

[19] Yeh D.-M., Huang C.-F., Chen C.-Y., Lu Y.-C. and Yang C. C., Nanotechnology **19**, 345201 (2008).

[20] Liu W., Wang X., Li Y., Geng Z., Yang F. and Li J., Sol. Ener. Mat. Sol. Cells **95**, 693 (2011).

[21] Nakayama K., Tanabe K. and Atwater H. A., Appl. Phys. Lett. **93**, 121904 (2008).

[22] Konda R. B., Mundle R., Mustafa H., Bamiduro O., Pradhan A. K., Roy U. N., Cui Y. and Burger A., Appl. Phys. Lett. **91**, 191111 (2007).

[23] Derkacs D., Chen W. V., Matheu P. M., Lim S. H., Yu P. K. L. and Yu E. T., Appl. Phys. Lett. **93**, 091107 (2008)

[24] Wurtz G. A., Pollard R., Hendren W., Wiederrecht G. P., Gosztola D. J., Podolskiy V. A. and Zayats A. V., Nat. Nanotechnol. **6**, 107 (2011).

[25] Pillai S., Catchpole K. R., Trupke T. And Green M. A., J. Appl. Phys. **101**, 093105 (2007).

[26] Beck . J., Mokkapati S. and Catchpole K. R., Prog. Photovolt: Res. Appl. **18**, 500 (2010).

[27] Temple T. L., Mahanama G. D. K., Reehal H. S. and Bagnall D. M., Sol. Ener. Mat. Sol. Cells **93**, 1978 (2009).

[28] Catchpole K. R. and Polman A., Appl. Phys. Lett. **93**, 191113 (2008).

[29] Beck F. J., Polman A. and Catchpole K. R., J. Appl. Phys. **105**, 114310 (2009).

[30] Ouyang Z., Pillai S., Beck F., Kunz O., Varlamov S., Catchpole K. R., Campbell P. and Green M. A., Appl. Phys. Lett. **96**, 261109 (2010).

[31] Mokkapati S., Beck F. J., Polman A. and Catchpole K. R., Appl. Phys. Lett. **95**, 053115 (2009).

[32] Schmid M., Klenk R., Lux-Steiner M. C., Topic M. and Krc J., Nanotechnology **22**, 025204 (2011).

[33] Beck F. J., Mokkapati S., Polman A. and Catchpole K. R., Appl. Phys. Lett. **96**, 033113 (2010).

[34] Yee K. S., IEEE Trans. Antennas Propag. **14**, 302 (1966).

[35] Purcell E. M. and Pennypacker C. R., Astrophys. J. **186**, 705 (1973).

[36] Bohren C. F. and Huffman D. R., Absorption and Scattering of Light by Small Particles (Wiley-VCH,Germany 1983).

[37] Kelly K. L., Coronado E., Zhao L. L. and Schatz G. C., J. Phys. Chem. B, **107**, 668-677 (2003).

[38] Jackson J. D., Classical Electrodynamics, p. 157 (John Wiley & Sons, USA 1999).

[39] Feldheim D. L. and Foss C. A., Metal Nanoparticles: Synthesis Characterization & Applications, p. 89-97 (Marcel Dekker, New York 2002).

[40] Novotny L. and Hecht B., Principles of Nano-Optics, p. 382-386, (Cambridge University Press, New York 2006).

[41] Sakurai J. J., Modern Quantum Mechanics,p. 89 (Addison-Wesley Publishing Company, USA 1994).

[42] Nalwa H. S., Handbook of Advanced Electronic and Photonic Materials and Devices, p.64 (Elsevier 2001).

[43] Atwater H. A. and Polman A. , Nature Materials **9**, 205 (2010).

[44] Stuart H. R., Hall D. G., J. Opt. Soc. Am. A **14**, 3001 (1997).

[45] Rayleigh L., Proc. London Math. Soc. **10**, 4 (1879).

[46] Jiran E. and Thompson C. V., jour. Elec. Mater. **19**, 1153 (1990).

[47] Nichols F. A. and Mullins W. W., Trans. Metall. Soc. AIME **233**, 1840 (1965).

[48] Srolovitz D. J. and Safran S. A., J. Appl. Phys. **60**, 247 (1986).

[49] Frantzeskakis E., Analysis of potential applications for the templated dewetting of metal thin films, p.18 (Thesis-Massachusetts Institute of Technology, Dept. of Materials Science and Engineering 2005).

[50] Trice J., Thomas D., Favazza C., Sureshkumar R. and Kalyanaraman R., Phys. Rev. **75**, 235439 (2007).

[51] Hwang S.-J., Nix W. D. And Joo Y.-C., Acta Materialia **55**, 5297 (2007).

[52] Serrano A., Rodriguez de la Fuente O. And Garcia M. A., J. Appl. Phys. **108**, 074303 (2010).

[53] Chaudhari P., J. Appl. Phys. **45**, 4339 (1974).

[54] Chang C. Y. and Vook R. W., J. Mater. Res. **4**, 1172 (1989).

[55] Iwamura E., Ohnishi T. and Yoshikawa K., Thin Solid Films **270**, 450 (1995).

[56] Okamoto H., Subramanian P. R. and Kacprzak L., Binary Phase Diagrams, 2nd edition, (W.W. Scott, 1992).

[57] Olesinski R. W., Gokhale A. B. and Abbaschian G. J., J. Phase Equil. **10**, 635 (1989).

[58] Myroshnychenko V., Rodriguez-Fernandez J., Pastoriza-Santos I., Funston A. M., Novo C., Mulvaney P., Liz-Marzan L. M. and Garcia de Abajo F. J., Chem. Soc. Rev. **37**, 1792 (2008). & http://nanophotonics.csic.es/ index.php?option=com_wrapper&view= wrapper& Itemid=58, last accessed on 20/06/2011.

[59] Jiang Q., Tong H. Y., Hsu D. T., Okuyama K. and Shi F. G., Thin Solid Films **312**, 357 (1998).

[60] Lide D. R, Handbook of Chemistry and Physics, 80th edition, (CRCpress, Cleveland, OH, 1999-2000).

[61] Catchpole K. R. and Polman A., Opt. Express **16**, 21793 (2008).

[62] Micro Chemicals, "Wet Etching of Si.", www.microchemicals.eu/technical_information, (2009), last accessed on 13/04/2011.